Asian Journal of Pharmaceutical Sciences 21 (2026) 101120

Available online at www.sciencedirect.com

ScienceDirect

journal homepage: www.elsevier.com/locate/AJPS



Research Article

A novel mRNA nanovaccine with dual immunoregulation ameliorates rheumatoid arthritis and associated pneumonia

Jingjing Su[a], *Wenguang Huang*[a], *Wenying Zhang*[a], *Ziyi Wang*[a], *Hongzhou Gu*[b,*], *Pengchao Sun*[a,c,d,*], *Yongxing Zhao*[a,c,d,*]

[a] *School of Pharmaceutical Sciences, Zhengzhou University, Zhengzhou 450001, China*
[b] *Department of Chemical Biology, School of Chemistry and Chemical Engineering, Frontier Sciences Center for Transformative Molecules, and National Center for Translational Medicine, Shanghai Jiao Tong University, Shanghai 200240, China*
[c] *Henan Key Laboratory of Nanomedicine for Targeting Diagnosis and Treatment, Zhengzhou 450001, China*
[d] *Key Laboratory of Advanced Drug Preparation Technologies, Ministry of Education of China, Zhengzhou University, Zhengzhou 450001, China*

ARTICLE INFO

Article history:
Received 21 July 2025
Revised 25 October 2025
Accepted 28 November 2025
Available online 10 January 2026

Keywords:
Rheumatoid arthritis
Pneumonia
mRNA nanovaccine
Immunoregulation

ABSTRACT

Rheumatoid arthritis (RA) as a systemic autoimmune disease, frequently triggers various extra-articular symptoms, particularly the RA-associated pneumonia. Unfortunately, the RA-associated pneumonia has garnered insufficient attention, and conventional RA therapies may exacerbate pneumonia-related complications, thereby complicating the treatment process. Herein, a novel dual immunoregulatory mRNA nanovaccine (MPDA@RC@HM) is designed for the efficient treatment of RA and RA-associated pneumonia simultaneously. This innovative mRNA nanovaccine represents a highly organized nanostructure that integrates the rapamycin-loaded mesoporous polydopamine (MPDA) with mRNA encoding the epitope of type II collagen, and the surface is modified with hyaluronic acid and dendritic cell membrane. After intravenous injection into collagen-induced arthritis mice, the mRNA nanovaccine exhibits effective distribution and transfection within the spleen and lung, subsequently exerting potent immunoregulation in both organs, thereby yielding a dual therapeutic effect. This study presents a versatile mRNA nanovaccine platform for the treatment of autoimmune diseases and provides an innovative approach for addressing RA and RA-associated pneumonia.

© 2026 Shenyang Pharmaceutical University. Published by Elsevier B.V.
This is an open access article under the CC BY-NC-ND license (http://creativecommons.org/licenses/by-nc-nd/4.0/)

* Corresponding authors.
E-mail addresses: hongzhou.gu@sjtu.edu.cn (H. Gu), Pengchao_Sun@zzu.edu.cn (P. Sun), zhaoyx@zzu.edu.cn (Y. Zhao).
Peer review under responsibility of Shenyang Pharmaceutical University.

https://doi.org/10.1016/j.ajps.2026.101120
1818-0876/© 2026 Shenyang Pharmaceutical University. Published by Elsevier B.V. This is an open access article under the CC BY-NC-ND license (http://creativecommons.org/licenses/by-nc-nd/4.0/)

1. Introduction

Rheumatoid arthritis (RA) is a systemic chronic autoimmune disorder with potential to cause disability and even impact life expectancy [1]. Despite extensive research, the pathogenesis of RA remains incompletely elucidated. The intricate immune response in RA involves dysfunction in various immune cells, inflammatory cytokines and chemokines [2], thus greatly complicating the management of RA. More importantly, rheumatoid factor, autoantibodies and inflammatory cytokines frequently attack other organs, leading RA patients to suffer from a variety of extra-articular complications [3]. Approximately 10%−20% of RA patients develop clinically significant interstitial lung disease (ILD), predominantly manifesting as usual interstitial pneumonia and non-specific interstitial pneumonia [4]. This condition consequently exacerbates pulmonary fibrosis, impairs lung function, and even increases mortality [5]. Nevertheless, the optimal treatment strategies for RA and RA-associated pneumonia remain inadequately investigated, and some commonly prescribed clinical medications may further exacerbate the progress of RA-associated pneumonia. For example, the first-line anti-RA drug methotrexate poses potential lung toxicity, while inappropriate use of immunosuppressive biologic disease-modifying antirheumatic drugs elevates the risk of lung infections [6]. Therefore, there is an urgent need for the development of innovative treatments that can specifically suppress both RA and RA-associated pneumonia.

One potential solution is to establish immune tolerance and reduce the stimulation of autoantibodies and inflammatory cytokines to both joints and lungs by alleviating the systemic immune response, while avoiding possible side effects on the lungs. Messenger RNA (mRNA) vaccines have demonstrated their effectiveness in modulating immune responses and have been widely used in the treatment of cancers, lung infections and autoimmune diseases [7]. mRNA vaccines function by directly delivering mRNA encoding a specific antigen to the target cells, and the mRNA is then translated into the intended antigen through the protein synthesis system, subsequently eliciting a specific immune response [8]. For instance, mRNA encoding $MOG_{35–55}$, encapsulated in lipid nanoparticles (LNPs), elicited systemic immune tolerance by targeting splenic antigen-presenting cells (APCs) for multiple sclerosis treatment [9]. Similarly, mRNA encoding peanut allergen epitopes effectively promoted the production of Treg and suppressed Th2 immunity, thereby alleviating anaphylaxis [10]. Encouraged by these findings, the development of a novel mRNA encoding pathogenic autoantigen for RA emerges as a promising strategy to mitigate the systemic immune responses and consequently reverse the development of RA and RA-associated pneumonia [11].

Type II collagen (CII) is a major component of articular cartilage tissue [12]. The presence of elevated levels of antibodies against CII in both the serum and synovial fluid of RA patients at the early stages strongly suggests that the specific immunity against CII plays a substantial role in the onset of RA [13]. Intravenous administration of a DNA vaccine encoding the whole CII effectively elevated the Treg population in the peripheral blood of collagen-induced arthritis (CIA) mice, thereby inducing immune tolerance [14]. Nevertheless, this approach may be accompanied by a potential risk of genomic integration. Notably, the epitope composing amino acids 250-270 of CII ($CII_{250–270}$) possesses the capability to elicit the response of specific T cells, serving as the primary active fragment that triggers the autoimmune response [15,16]. Although oral administration of peptide $CII_{250–270}$ was effective in inhibiting specific cellular and humoral responses in CIA mice [17], significant effort is required to address the limitations of the peptide vaccine and the challenges faced by the peptide vaccine in the gastrointestinal system before it fully functions. Hence, an mRNA vaccine specifically encoding $CII_{250–270}$ is promising to yield superior therapeutic efficacy.

However, mRNA is frequently susceptible to the nuclease *in vivo*, potentially causing a loss of activity before reaching APCs, such as dendritic cells (DCs), thereby resulting in the failure of immune regulation. To ensure that the mRNA encoding $CII_{250–270}$ exerts a robust systemic immunoregulation for the treatment of RA and RA-associated pneumonia, it is essential to develop an mRNA nanovaccine platform to guarantee the delivery of mRNA to DCs in the spleen, which serves as the pivotal immunoregulatory hub within the body [18]. Mesoporous polydopamine (MPDA) has been extensively utilized as the carrier of drugs for the treatment of various diseases due to its abundant mesoporous structure and satisfactory biocompatibility [19]. Moreover, the efficient reactive oxygen species (ROS) clearance capability of MPDA contributes to its exceptional degradability at the site of disease, rendering MPDA an ideal drug carrier [20]. Particularly, the ROS scavenging ability of MPDA holds the potential to relieve the oxidative stress of mature DCs and induce DC tolerance phenotype [21]. Additionally, the codelivery of relevant autoantigens and immunosuppressant rapamycin (Rapa) to DCs is a powerful strategy to enhance immune tolerance for the treatment of autoimmune diseases [22]. Rapa and Aβ peptide co-loaded LNPs promoted antigen-specific tolerance of DCs, thereby alleviating neuroinflammation of Alzheimer's disease [23]. Furthermore, DC membrane biomimetic technology has the potential to facilitate the precise delivery of the mRNA nanovaccine to DCs *via* homologous targeting [24]. By leveraging the abundant DCs in the spleen and the inflammatory lungs [25], a DC membrane functionalized mRNA nanovaccine platform can efficiently accumulate in the spleen and lungs, thereby achieving dual immunoregulation.

Herein, a novel mRNA nanovaccine (MPDA@RC@HM) with dual immunoregulation for the spleen and lungs is developed to achieve simultaneous treatment of RA and RA-associated pneumonia (Fig. 1) for the first time. For this purpose, mRNA encoding $CII_{250–270}$ (CII mRNA, C) was designed and fabricated, which was later adsorbed onto MPDA with the aid of a cationic lipid DOTAP. To boost the immune tolerance, Rapa was encapsulated in the nanocarrier MPDA ahead of mRNA loading (MPDA@RC). In addition, the surface of the MPDA@RC was functionalized with hyaluronic acid (HA) and DC membrane in turn to produce the final mRNA nanovaccine MPDA@RC@HM (Fig. 1), which could

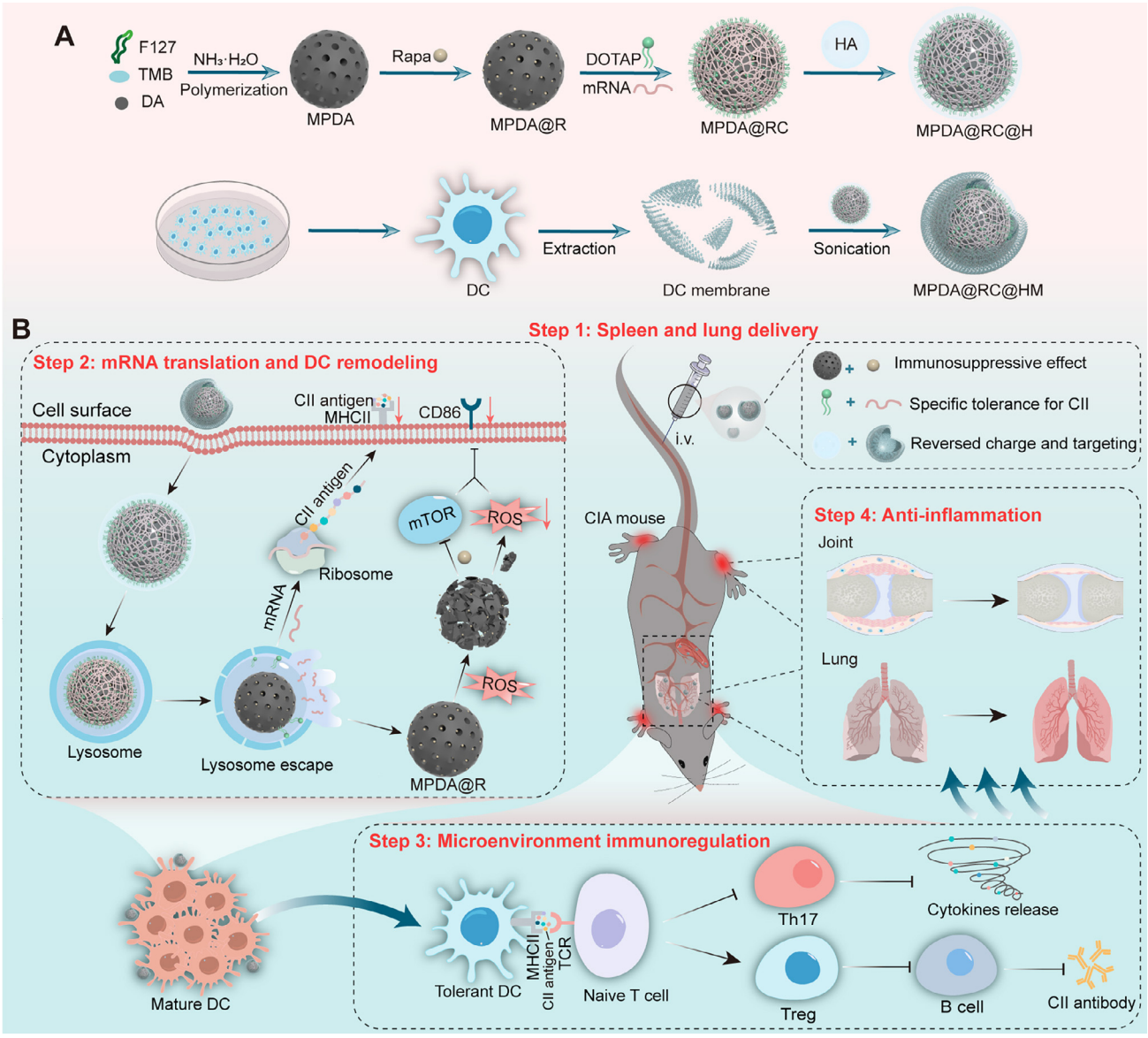


Fig. 1 – Preparation and possible anti-inflammatory mechanisms of the mRNA nanovaccine (MPDA@RC@HM) for the treatment of RA and RA-associated pneumonia. (A) Schematic illustration of the synthesis of the mRNA nanovaccine with a multi-layer assembly structure; (B) Possible dual immunoregulation mechanisms in CIA mice. The mRNA nanovaccine was injected intravenously into CIA mice and delivered precisely to the spleen and lungs. After entering DCs within the inflammatory microenvironment, the mRNA nanovaccine successfully escaped from the lysosome and expressed the target antigen in the cytoplasm. MPDA and Rapa promoted a tolerance phenotype for DCs, thereby inhibiting the activation of downstream immune cells and reducing the production of autoantibodies and inflammatory cytokines.

achieve efficient accumulation in the organs of interest and subsequent translation of mRNA. Meanwhile, to establish a universal mRNA nanovaccine platform and evaluate its *in vitro* and *in vivo* transfection efficiency, enhanced green fluorescent protein (EGFP, E) mRNA-loaded MPDA@RE@HM and firefly luciferase (LUC, L) mRNA-loaded MPDA@RL@HM were synthesized *via* identical preparation method. Our results demonstrated that the designed mRNA nanovaccine platform was successfully delivered to spleen and lung, and the loaded mRNA was then efficiently translated within these organs. The mRNA nanovaccine MPDA@RC@HM encapsulating CII mRNA efficiently eliminated ROS within inflammatory DCs and induced DC tolerance. Additionally, MPDA@RC@HM successfully rebalanced the Treg/Th17 ratio in both the spleen and lung of CIA mice, facilitating extensive modulation of the immune response throughout the body, particularly in inflammatory joint and lung. The present study not only pioneers a novel therapeutic approach for the efficient treatment of RA and RA-associated pneumonia but also provides a universal mRNA nanovaccine platform for mRNA-based therapy of other autoimmune diseases.

2. Materials and methods

2.1. Materials

Gel extraction kit was purchased from Omega Bio-tek (Norcross, USA). T7 RNA transcription kit and vaccinia capping system were bought from Novoprotein (Shanghai, China). The 1-methylpseudouridine-5′-triphosphate (m1-ΨTP) was obtained from Trilink Biotechnologies (San Diego, USA). Cy5-labeled uridine triphosphate (UTP) was obtained from ApexBio Technology (Houston, USA). BCA protein assay kit and DNase I were purchased from Solarbio Science & Technology (Beijing, China). Fetal bovine serum (FBS) was supplied from VivaCell Biosciences (Shanghai, China). Low range ssRNA ladder was bought from New England Biolabs (Ipswich, USA). Dopamine hydrochloride (DA·HCl) was obtained from Adamas (Basel, Switzerland). Pluronic F127, 1,3,5-trimethylbenzene (TMB, ≥98.0%) and fluorescein isothiocyanate (FITC) were bought from Aladdin (Shanghai, China). Rapa (≥98.0%), CCK-8 and D-Luciferin potassium salt (≥98%) were purchased from MeilunBio (Dalian, China). Lipofectamine messenger reagent and Quant-iT^{TM} RiboGreen^{TM} RNA reagent were obtained from Thermo Fisher Scientific (Waltham, USA). The 2,2′-azino-bis (3-ethylbenzothiazoline-6-sulfonic acid) diammonium salt (ABTS, 98%) and sodium phosphotungstate (99%) were obtained from Macklin Biochemical (Shanghai, China). DOTAP chloride (≥98.0%) and 2′,7′-DCFH-DA were purchased from MedChemExpress (Shanghai, China). DNA Ladder (0.1–10 kb) and 1,1′-dioctadecyl-3,3,3′,3′-tetramethylindocarbocyanine perchlorate (DiI) were bought from Beyotime Biotechnology (Shanghai, China). Recombinant human interferon-γ (IFN-γ), Granulocyte macrophage-colony stimulating factor (GM-CSF), and IL-4 were supplied by PeproTech (USA). Chicken type II collagen (2 mg/ml), complete freund's adjuvant (4 mg/ml), incomplete freund's adjuvant, and mouse type II collagen IgG antibody ELISA kits were purchased from Chondrex (Woodinville, USA). Primers were synthesized by Sangon Biotech (Shanghai, China). BV510 anti-mouse majorhistocompatibility complex (MHC) II, PerCP-Cy5.5 anti-mouse CD3e, Alexa Fluor 647 anti-mouse Foxp3, BB515 anti-mouse CD25 and PE anti-mouse IL-17A were purchased from BD Bioscience (Franklin Lake, USA). PE/Cy7 anti-mouse CD4, Alexa Fluor 700 anti-mouse CD45, BV421 anti-mouse CD86, PE anti-mouse CD11c and FITC anti-mouse MHCII were purchased from Biolegend (San Diego, USA). TRIzon reagent was obtained from Cwbiotech (Jiangsu, China). Dispase was purchased from Maokangbio (Shanghai, China). LysoTracker Green DND-26, Reverse transcription kit, SYBR green master mix, and Collagenase I were bought from Yeasen Biotechnology (Shanghai, China).

2.2. Cells and animals

DC2.4 (a murine DC line) obtained from iCell (Shanghai, China) were cultured in RPMI 1640 medium supplemented with 10% FBS. Cultures were maintained at 37 °C in a humidified incubator with 5% of CO_2. Seven-week-old male DBA/1 mice were purchased from Cavens (SCXK (Su) 2021-0013, Jiangsu, China). All animal experiments were conducted in accordance with the Guidelines for Care and Use of Laboratory Animals, approved by the Animal Ethics Committee of the School of Pharmaceutical Sciences, Zhengzhou University (license: yxyllsc20240058).

2.3. mRNA design and synthesis

CII mRNA was designed based on the CII epitope peptide 250-270 (GPKGQTGKPGIAGFKGEQGPK) [17], which was later fused to an upstream signal peptide (SP) domain (MRVTAPRTLILLLSGALALTETWAGS) and a downstream MHC class I trafficking signal (MITD) domain (IVGIVAGLAVLA VVVIGAVVATVMCRRKSSGGKGGSYSQAASSDSAQGSDVSLTA) as previously described [26]. The gene sequences encoding these domains were cloned into a recombinant plasmid containing T7 promoter, 5′-untranslated regions (UTR), 3′-UTR and polyA tail, and the primary sequences were listed in Table S1. The designed plasmid was first linearized using a restriction endonuclease, followed by purification with a gel extraction kit. For *in vitro* transcription, UTP was replaced by m1-ΨTP to improve the stability and reduce the immunogenicity of mRNA according to the manufacturer's instructions of the T7 RNA transcription kit. Finally, the mRNA was capped at the 5′-end with the vaccinia capping system. The resulting mRNA was purified by the LiCl precipitation method. EGFP mRNA and LUC mRNA were synthesized using the same plasmid template as CII mRNA. Cy5-labeled EGFP mRNA (^{Cy5}E) was obtained by adding Cy5-labeled UTP during *in vitro* transcription.

2.4. Preparation of MPDA nanoparticles

Pluronic F127 (1.0 g) and dopamine hydrochloride (0.5 g) were dissolved in a mixture of ethanol (50 ml) and deionized water (50 ml), followed by stirring at room temperature for 15 min. Subsequently, 1.5 mL of TMB was added dropwise to the above solution and stirred at 800 rpm for 30 min. Then, 5 mL of ammonia was introduced and stirring for an additional 30 min. The reaction mixture was then centrifuged (13,000 rpm, 30 min) and the resulting precipitate was resuspended in the mixture of ethanol/acetone (2:1, v/v). The templates Pluronic F127 and TMB were removed by sonication (200 W, 10 min) and centrifugation (13,000 rpm, 10 min), alternately three times to obtain MPDA. MPDA was later resuspended in deionized water and stored at 4 °C for further experiments.

2.5. Loading of Rapa on MPDA

Rapa was dissolved into ethanol at concentrations of 0.4, 0.8, 1.2, 1.6 and 2 mg/ml. Rapa (250 μl) at varying concentrations was later mixed with 3 ml MPDA (0.5 mg/ml) and stirred at room temperature for 12 h in the dark. Subsequently, the mixture was centrifuged at 20,000 rpm for 5 min and washed with nuclease-free water three times to remove the free Rapa. All supernatant was collected and the absorbance at 278 nm was recorded using UV-vis spectrophotometer (Shimadzu, Japan). The loading efficiency was calculated according to

Eq. 1:

$$\text{Loading efficiency } (\mu g/mg) = \frac{M_{\text{Total Rapa}} - M_{\text{Free Rapa}}}{M_{\text{MPDA}}} \quad (1)$$

Where $M_{Total\ Rapa}$ was the mass of added Rapa, $M_{Free\ Rapa}$ was the mass of Rapa in the supernatant and M_{MPDA} was the mass of feeding MPDA.

2.6. Preparation of DOTAP+E

DOTAP was dissolved into ethanol to obtain the 2 mg/ml stock solution. DOTAP solution (2 mg/ml) and EGFP mRNA (250 ng/μl) were mixed in the mass ratios of 1:1, 2:1, 4:1, 6:1, 8:1 and 10:1, followed by vortexing at a low speed for 5 s. The mixture was incubated at room temperature for 20 min to obtain DOTAP+E with various mass ratios.

2.7. Preparation of DC membrane

The cell membrane was extracted from DC2.4. Briefly, DC2.4 were collected and washed with PBS twice and lysed (20 mM Tris HCl (pH 7.5), 10 mM KCl, 2 mM $MgCl_2$ and 0.1 mM phenylmethylsulfonyl fluoride) for 30 min on ice, followed by sonication to completely rupture the cells. The cell suspension was centrifuged at 4 °C (700 g, 10 min) to collect the membrane supernatant, which was subjected to high-speed centrifugation (14,000 g, 10 min) to obtain the DC membrane precipitation. The DC membrane was next washed with RNase-free water twice to remove the residual protein. The concentration of the total membrane protein was quantified by the Bradford protein assay. The resulting membrane was stored at −80 °C for further use.

2.8. Preparation of the mRNA nanovaccine platform

To prepare MPDA@RE, MPDA@R (1 mg/ml) was thoroughly mixed with varying volumes of DOTAP stock solution (2 mg/ml). The mixture was sonicated at 200 W for 10 min, followed by the addition of an equal volume of mRNA solution (250 ng/μl) to achieve DOTAP-to-mRNA mass ratios of 4:1, 6:1, 8:1 and 10:1. The resulting mixtures were incubated at room temperature for 20 min to obtain MPDA@RE. For subsequent experiments, a DOTAP-to-mRNA mass ratio of 10:1 was selected. To fabricate MPDA@RE@H, MPDA@RE was mixed with varying volumes of HA solution (4 mg/ml) and incubated at room temperature for 30 min to yield MPDA@RE@H. The mass ratio of DOTAP to HA was determined to be 1:4 to prepare MPDA@RE@H for subsequent use. MPDA@RE@HM was prepared using an ultrasound method [27]. Briefly, the varying volumes of DC membrane were added to the MPDA@RE@H sample and sonicated at 80 W for 3 min in ice bath. A mass ratio of MPDA to DC membrane of 1:2 was used for subsequent experiments.

2.9. Characterization

The loading capacity of mRNA on different samples was analyzed with agarose gel electrophoresis assay, and the encapsulation efficiency of mRNA was detected by Quant-iT™ RiboGreen™ RNA Reagent according to the manufacturer's instructions and calculated according to Eq. 2:

$$\text{Encapsulation efficiency } (\%) = \frac{M_{\text{Total mRNA}} - M_{\text{Free mRNA}}}{M_{\text{Total mRNA}}} \times 100\% \quad (2)$$

Where $M_{Total\ mRNA}$ was the mass of added mRNA, $M_{Free\ mRNA}$ was the mass of mRNA in the supernatant.

The hydrodynamic diameter and zeta potential of different preparations were measured using the Zetasizer Nano-ZS system (Malvern, UK). Transmission electron microscope (TEM) was performed using a 120 kV Talos L120C microscope (Thermo Fisher Scientific, USA). Samples containing mRNA were dropwise added onto the copper meshes and subjected to negative staining with 2% sodium phosphotungstate solution for 30 s and then washed with water three times, followed by air drying to obtain the TEM images.

Sodium dodecyl sulfate-polyacrylamide gel electrophoresis (SDS-PAGE) was later employed to map DC membrane proteins. MPDA@RE@H, MPDA@RE@HM, and DC membrane were mixed with 4× protein loading buffer, respectively, denaturized at 95 °C for 5 min and loaded onto SDS-PAGE. The protein gel was run at 300 V for 20 min, followed by staining with coomassie brilliant blue R-250. The gel was captured by Gel Doc XR$^+$ imaging system (Bio-rad, USA).

The non-specific adsorption of serum proteins onto different preparations was examined with the same method. MPDA@RE, MPDA@RE@H and MPDA@RE@HM were dispersed in RPMI 1640 medium containing 10% FBS and incubated at 37 °C for 1 h. After centrifugation (20,000 rpm, 5 min), the precipitates were washed with water three times to remove unbound serum proteins. The obtained samples were resuspended in water, mixed with 4× loading buffer, denaturized at 95 °C for 5 min and analyzed by SDS-PAGE.

For co-localization analysis, 400 μl MPDA@R (0.5 mg/ml) was stirred with 30 μl FITC (0.2 mg/ml) overnight in the dark. The product was washed with RNase-free water to remove the free FITC until the supernatant was clear. Additionally, 10 μM of DiI was added into the DC membrane and incubated at 37 °C for 8 min in the dark. The DiI-labeled membrane was washed with RNase-free water to remove the unbound membrane dye. Subsequently, the FITC-labeled MPDA@R, DiI-labeled membrane, and Cy5-labeled EGFP mRNA were used to prepare MPDA@RE@HM, and the fluorescent mRNA nanovaccine was observed using confocal laser scanning microscopy (CLSM, Leica TCS SP8, Germany). The corresponding co-localization analysis was performed using ImageJ.

2.10. In vitro transfection

DC2.4 were seeded into 12-well plates (6×10^4 cells per well) and incubated at 37 °C and 5% CO_2 for 24 h. The cultured medium was replaced with RPMI 1640 medium (10% FBS) containing various formulations and incubated for 48 h. The final concentration of different ingredients was equivalent to MPDA@RE@HM (5 μg/ml, calculated as the mass concentration of MPDA). The expression of EGFP was first captured *via* a fluorescence microscope (Motic AE31 EF-

INV, China). Subsequently, the cells were washed with PBS three times and digested with trypsin-EDTA, followed by quantification of the fluorescence intensity of EGFP with a flow cytometer (BD LSRFortessa).

2.11. Cell viability

To investigate the impact of various preparations on the cell viability of normal DC2.4, DC2.4 were seeded into 96-well plates (6×10^3 cells per well) and incubated for 24 h. The digested medium was then replaced with fresh medium containing MPDA, Rapa, MPDA@R, DOTAP, MPDA@RC, MPDA@RC@H and MPDA@RC@HM with different concentrations (2, 5 and 10 μg/ml, final concentration calculated by the mass of MPDA; the concentration of Rapa and DOTAP was equivalent to MPDA@RC@HM), respectively. 48 h later, the medium was replaced with 100 μl RPMI 1640 medium including 4% CCK-8 (v/v) and incubated for another 3 h at 37 °C. The absorbance at 450 nm was detected via Synergy H1 microplate reader (Bio-Tek, USA). To assess the impact of various preparations on inflammatory DC2.4 viability, DC2.4 were firstly cultured in 96-well plates (6×10^3 cells per well) for 24 h and then incubated with 100 ng/ml of IFN-γ for another 24 h [28], followed by treatment with different preparations. The cell viability was calculated according to Eq. 3:

$$\text{Cell viability (\%)} = \frac{A_s - A_0}{A_b - A_0} \times 100\% \quad (3)$$

Where A_s was the absorbance of the experimental sample, A_b was the absorbance of the blank cells, and A_0 was the absorbance of the background.

2.12. Cellular uptake

DC2.4 were seeded into the 24-well plates (3×10^4 cells per well) and cultured for 24 h. The culture medium was replaced with 500 μl IFN-γ (100 ng/ml) to induce inflammation. After incubation for 24 h, the cells were cultured with DOTAP+^{Cy5}E, MPDA@R^{Cy5}E, MPDA@R^{Cy5}E@H and MPDA@R^{Cy5}E@HM (5 μg/ml). After treatment for 0.5, 1, 2 and 4 h, the cells were washed with PBS twice and fixed with 4% paraformaldehyde for 10 min, followed by incubating with 400 μl DAPI (1 μg/ml) for 10 min in the dark. After washing the cells with PBS three times, the cellular Cy5 was captured by CLSM and quantitatively analyzed by ImageJ. For flow cytometry analysis, DC2.4 were seeded into the 12-well plates (6×10^4 cells per well) and incubated with 100 ng/ml IFN-γ. The inflammatory DC2.4 were next treated with different preparations for 2 h. Then the cells were washed with PBS and collected for flow cytometer analysis (BD Biosciences, USA).

2.13. Lysosome escape

DC2.4 were seeded into the confocal dishes (35 mm diameter) at a density of 6×10^4 cells per dish and cultured in RPMI 1640 complete medium for 24 h. The cells were then incubated with IFN-γ (100 ng/ml) for 24 h. Subsequently, 1 ml MPDA@R^{Cy5}E@HM (5 μg/ml) was added and incubated with the cells for 1, 2, 4 and 6 h, respectively. After incubation, the cells were washed twice with PBS and treated with 700 μl LysoTracker Green (75 nM) at 37 °C in the dark, followed by Hoechst staining (2 μg/ml) for 15 min. Finally, the cells were washed twice with PBS and imaged using CLSM.

2.14. Free radical scavenging ability

The total antioxidant capacity was detected *via* ABTS assay [29]. ABTS (7.4 mM) was reacted with an equal volume of potassium persulfate solution (2.6 mM) for 16 h in the dark. Then the mixture was diluted with deionized water to obtain the ABTS working solution. A volume of 40 μl MPDA or MPDA@R with different concentrations was mixed subsequently with 360 μl ABTS working solution and incubated for 20 min at 37 °C in the dark. After centrifugation, the supernatant was collected and the absorbance at 734 nm was measured. ABTS· scavenging ability was calculated as Eq. 4:

$$\text{ABTS}\cdot \text{ radical scavenging rate (\%)} = \frac{A_b - A_S}{A_b - A_0} \times 100\% \quad (4)$$

where A_b was the absorbance of the ABTS· solution without the samples, A_S was the absorbance of the ABTS· solution with the samples, A_0 was the absorbance of the solution without ABTS· and samples.

The ·OH scavenging ability of MPDA and MPDA@R was measured by 3,3′,5,5′-Tetramethylbenzidine assay [30]. A volume of 60 μl MPDA or MPDA@R solution with different concentrations was mixed with $FeSO_4 \cdot 7H_2O$ (0.01 mM) and H_2O_2 (0.1 mM) in NaAC–HAC buffer (pH 4.5) and incubated for 6 h at 37 °C in the dark. After centrifugation, the supernatant was incubated with an equal volume of 3,3′,5,5′-tetramethylbenzidine for 5 min, and the absorbance at 652 nm was then measured. The ·OH scavenging ability was calculated by Eq. 5:

$$\cdot\text{OH radical scavenging rate (\%)} = \frac{A_b - A_S}{A_b - A_0} \times 100\% \quad (5)$$

Where A_b was the absorbance of the reaction solution without the samples, A_S was the absorbance of the reaction solution with the samples, and A_0 was the absorbance of the reaction solution without H_2O_2 and samples.

2.15. Influences on cellular ROS

DC2.4 were seeded into 12-well plates (6×10^4 cells per well) and cultured for 24 h at 37 °C. After IFN-γ stimulation, the cells were incubated with MPDA, Rapa, MPDA@R, MPDA@RC, MPDA@RC@H or MPDA@RC@HM at a final concentration of 5 μg/ml for 48 h. After incubation, the cells were washed twice with PBS, treated with 10 μM DCFH-DA, and incubated for 30 min at 37 °C in the dark. Finally, the cells were harvested and analyzed by flow cytometer.

2.16. In vitro immunosuppressive effect

IFN-γ-induced DC2.4 were cultured with different preparations for 48 h. Subsequently, the cells were collected

and washed with PBS twice and then stained with PE anti-mouse CD86 and BV510 anti-mouse MHCII for 30 min at 4 °C. After being washed twice with PBS, the cells were analyzed by flow cytometer. Bone marrow cells were harvested from mouse femurs and tibias and red blood cells (RBCs) were removed with ACK lysis buffer. The cells were then resuspended at a density of 1×10^6 cells/mL in RPMI 1640 medium containing 10% FBS, 15 ng/ml GM-CSF, and 10 ng/ml IL-4. Half of the culture medium was replaced with fresh medium containing GM-CSF and IL-4 every 2 d. After 6 d, the resulting bone marrow-derived dendritic cells (BMDCs) were reseeded into 12-well plates (6×10^5 cells per well) and treated with lipopolysaccharide (LPS, 1 μg/ml) and various preparations (5 μg/ml) for 24 h. BMDCs were next collected and stained with Alexa Fluor 700 anti-mouse CD45, BV421 anti-mouse CD86, PE anti-mouse CD11c, and FITC anti-mouse MHCII for flow cytometry analysis.

2.17. *Establishment of CIA mice model*

After acclimatizing for 1 week, the DBA/1mice were injected with 100 μl emulsion containing chicken type II collagen and complete freund's adjuvant subcutaneously in the base of the tail on Day 0 for the first immunization. On Day 21, 100 μl emulsion consisting of chicken type II collagen and incomplete freund's adjuvant was injected subcutaneously to boost the immunization. The swelling, erythema and joint flexibility of the paws of the mice were monitored. The arthritis scores of four feet were calculated to evaluate the development of joint inflammation [31].

2.18. *Anti-RA efficacy of the mRNA nanovaccine in CIA mice*

To evaluate the efficacy of the mRNA nanovaccine in inhibiting arthritis in CIA mice, the CIA mice were divided into seven groups on Day 30 ($n = 6$ per group) and treated with MPDA@R (80 μg per mouse), DOTAP+C, MPDA@RC, MPDA@RC@H, MPDA@RC@HM and MPDA@RL@HM (equivalent to 20 μg mRNA per mouse) every 4 d (four administrations in total). Untreated CIA mice served as the model group, while healthy mice were designated as the blank group. During the treatment period, the body weight, paw thickness and arthritis scores were measured every 2 d. To assess the damage of joint bone tissue in CIA mice after different treatment groups, the joints of the mice were collected for micro-computed tomography (micro-CT) analysis (Bruker SkyScan1276, Germany) on Day 47. The resulting images were reconstructed in three dimensions. All samples were scanned with a 0.25 mm aluminum filter. The source voltage, current, total rotation and rotation step of micro-CT were set at 55 kV, 200 μA, 360° and 0.3°, respectively. Additionally, the histomorphometric indexes, including bone mineral density (BMD), bone volume/tissue volume (BV/TV) and trabecular thickness (Tb.Th), were quantitatively detected. Moreover, the ankle joint of mice was stained with hematoxylin-eosin (H&E) and safranin O-fast green (S&F) to evaluate the extent of joint inflammation and bone/cartilage destruction, and the images were obtained via a microscope. The histopathological scoring was conducted as previously described [32].

2.19. *Systemic immunomodulation mechanism in CIA mice*

To analyze the phenotype of T cells in the spleen, the fresh splenocytes of CIA mice were prepared on Day 47, and ACK lysis buffer was used to remove RBCs. Splenocytes were treated with leukocyte activation cocktail and incubated in a cell culture incubator for 5 h. Subsequently, the cells were collected and stained with PE/Cy7 anti-mouse CD4, Alexa Fluor 700 anti-mouse CD45, PerCP-Cy5.5 anti-mouse CD3e, and BB515 anti-mouse CD25 at 4 °C for 30 min. Moreover, the cells were fixed and permeabilized using a transcription factor buffer set according to the manufacturer's instructions and then stained with Alexa Fluor 647 anti-mouse Foxp3 and PE anti-mouse IL-17A for flow cytometry analysis.

For RT-qPCR and ELISA analysis, the ankles of mice were collected on Day 47 and treated with TRIzon reagent to extract the entire RNA. The reverse transcription kit was used to remove the genome from the extracted mRNA and synthesize the complementary DNA (cDNA). Then, RT-qPCR assay was conducted in accordance with the manufacturer's instructions. Relative expression of mRNA was normalized to GAPDH, and the sequences of the primers were listed in Table S2. For ELISA analysis, the fresh serum of mice was centrifuged (10,000 rpm, 3 min) to remove the insoluble components. Anti-CII antibody levels were measured using mouse type II collagen IgG antibody ELISA kits according to the manufacturer's instructions.

To assess the biocompatibility of mRNA nanovaccine in CIA mice, the fresh whole blood of mice was collected on Day 47 to detect the levels of RBC, white blood cell (WBC), hemoglobin (HGB), hematocrit (HCT) and platelet (PLT) by blood cell analyzer (Mindray BC-5180, China). The major organs including the heart, liver, spleen, lung and kidney were harvested and fixed in 4% paraformaldehyde solution for H&E staining to assess the possible pathological damage. After staining, the slices were imaged via a microscope.

2.20. *Biodistribution and bioluminescence imaging of the mRNA nanovaccine in CIA mice*

Cy5-labeled EGFP mRNA was used to prepare DOTAP+^{Cy5}E, MPDA@R^{Cy5}E, MPDA@R^{Cy5}E@H and MPDA@R^{Cy5}E@HM to investigate the biodistribution of the mRNA nanovaccine platform. CIA mice were randomly divided into four groups and injected with DOTAP+^{Cy5}E, MPDA@R^{Cy5}E, MPDA@R^{Cy5}E@H, or MPDA@R^{Cy5}E@HM (equivalent to 20 μg mRNA per mouse). After intravenous injection, the mice were imaged via the IVIS imaging system (PerkinElmer, USA) at various time points.

LUC mRNA was used to prepare DOTAP+L, MPDA@RL, MPDA@RL@H and MPDA@RL@HM, which were intravenously injected into CIA mice (equivalent to 20 μg mRNA per mouse) to evaluate the transfection efficiency of the mRNA nanovaccine platform. After 6 h, the mice received an intraperitoneal injection of D-luciferin in Dulbecco's PBS (150 mg/kg) 10 min prior to imaging using the IVIS imaging system.

2.21. Therapeutic effects of the mRNA nanovaccine on RA-associated pneumonia

To assess the respiratory capacity, the CIA model was first established, and the CIA mice were divided into two groups on Day 30: the model group and the MPDA@RC@HM group. Healthy mice were set as the blank group. Starting on Day 30, the mice were measured every 2 d using a whole-body non-invasive plethysmography system (HRH-LFM20, China). The flowmeter was adjusted to 1 l/min and then the body plethysmograph was calibrated. The mice were put into the body plethysmograph and the respiratory signals of the mice were collected every 5 s after the mice were silenced. The average value of each parameter was calculated within 1 min. The fresh lung samples were collected on Day 47, and frozen-sliced for dihydroethidium (DHE) staining to assess ROS levels and H&E staining to evaluate the alveolar pathological damage. Masson staining was performed on fixed lung tissues to assess the degree of fibrosis based on the proportion of blue-stained area. The images were obtained via a slice scanner (3DHISTECH Pannoramic, Hungary).

2.22. Pulmonary microenvironment remodeling in RA-associated pneumonia

To detect the total protein content and cell count in bronchoalveolar lavage fluid (BALF), the trachea of mice was exposed after dissection, and 1 mL ice-cold PBS was slowly injected into the lung using an intravenous indwelling needle, remaining for 10 s. Following three repeated injections, the BALF was collected. The BALF was next centrifuged (4 °C, 800 g, 10 min) to collect the supernatant for total protein content determination by the BCA protein assay kit. The number of cells in the pellet was quantified by a cell counter (Countstar Mira BF, China) after the removal of RBCs with ACK lysis buffer.

To analyze the immune cell composition via flow cytometer, lung tissue dissociation was initially performed as previously described [33]. Fresh lung tissue was washed several times with Hank's balanced salt solution, minced into small pieces, and immersed in the enzyme dissociation solution (500 U/ml collagenase I, 2.4 U/ml dispase and 0.33 U/ml DNase I in Hank's balanced salt solution). The mixture was incubated at 37 °C for 1 h, filtered through a 70-μm strainer, and centrifuged at 1,000 rpm for 5 min to obtain a cell pellet. The pellet was subsequently resuspended in ACK lysis buffer to remove RBCs. For T cell analysis, flow cytometry was performed in accordance with Section 2.19. For DC analysis, the cells were stained with Alexa Fluor 700 anti-mouse CD45 antibody, BV421 anti-mouse CD86 antibody, PE anti-mouse CD11c antibody, and FITC anti-mouse MHCII antibody at 4 °C for 30 min, and subsequently analyzed by flow cytometer.

For RNA-seq analysis, lung tissues were collected on Day 47 and preserved in RNA preservation solution. Total RNA extraction and quality assessment, cDNA library construction and sequencing using the Illumina NovaSeq 6000 platform were conducted by Biomarker Technologies Co., Ltd. (Beijing, China). Bioinformatics analysis was performed using BMKCloud (www.biocloud.net). Gene expression levels were calculated using the fragments per kilobase of transcript per million fragments mapped (FPKM) [34] method and subsequently analyzed with DESeq2 software. A threshold of fold change $\geq$1.5 and $P < 0.05$ was applied to identify differentially expressed genes (DEGs) between different groups. Kyoto Encyclopedia of Genes and Genomes (KEGG) and Gene Ontology (GO) enrichment analyses were performed to annotate DEGs. Gene Set Enrichment Analysis (GSEA) was conducted to compare all genes in the MPDA@RC@HM group with those in the model group, revealing trends in functional pathways and identifying key pathway-associated genes. The protein-protein interaction network was constructed using String (https://string-db.org/).

2.23. Statistical analysis

All results were expressed as mean ± standard deviation (SD). The statistical significance was assessed by one-way or two-way analysis of variance for multiple group comparisons using Tukey's or Dunnett test, and two-tailed unpaired t-tests for pairwise comparisons. The *P*-value smaller than 0.05 was considered statistically significant.

3. Results and discussion

3.1. Design, fabrication and characterization of mRNA and the mRNA nanovaccine platform

To design a stable mRNA that efficiently translated $CII_{250–270}$, a gene encoding $CII_{250–270}$ was first engineered and subsequently cloned into a recombinant plasmid, which incorporated the SP domain of MHC class I (upstream) and MITD domain (downstream) [26] (Fig. 2A). The recombinant plasmid was linearized (Fig. S1), transcribed *in vitro*, capped with cap1 structure at the 5′-end [35], and purified to obtain high-quality CII mRNA. To further enhance the translational capacity, UTP was substituted with m1-ΨTP during *in vitro* transcription [9]. Meanwhile, EGFP mRNA was synthesized using the same method to assess the translation efficiency *in vitro* of the designed mRNAs according to a well-established strategy [10,36]. As shown in Fig. 2B, the migration rates of CII mRNA and EGFP mRNA in an agarose gel aligned with their theoretical sizes, illustrating successful *in vitro* transcription of the designed mRNAs. Subsequently, EGFP mRNA was transfected into DC2.4 with the assistance of a commercial transfection reagent (Lipofectamine messenger reagent) to verify the influence of m1-ΨTP modification on the translatability of the designed mRNA. As seen in Fig. S2, cells transfected with m1-ΨTP modified EGFP mRNA showed stronger fluorescence intensity than those transfected with unmodified EGFP mRNA. These results demonstrated that the designed mRNA was efficiently internalized by DC2.4 and successfully translated into the target protein. Moreover, the incorporation of m1-ΨTP modification was conducive to augmenting the translational capacity of the mRNA.

In order to safely and effectively deliver CII mRNA for further application *in vivo*, a universal mRNA delivery platform was fabricated using MPDA as the carrier. Meanwhile, an immune regulator Rapa was co-loaded into MPDA, which aimed to remodel the inflammatory microenvironment along

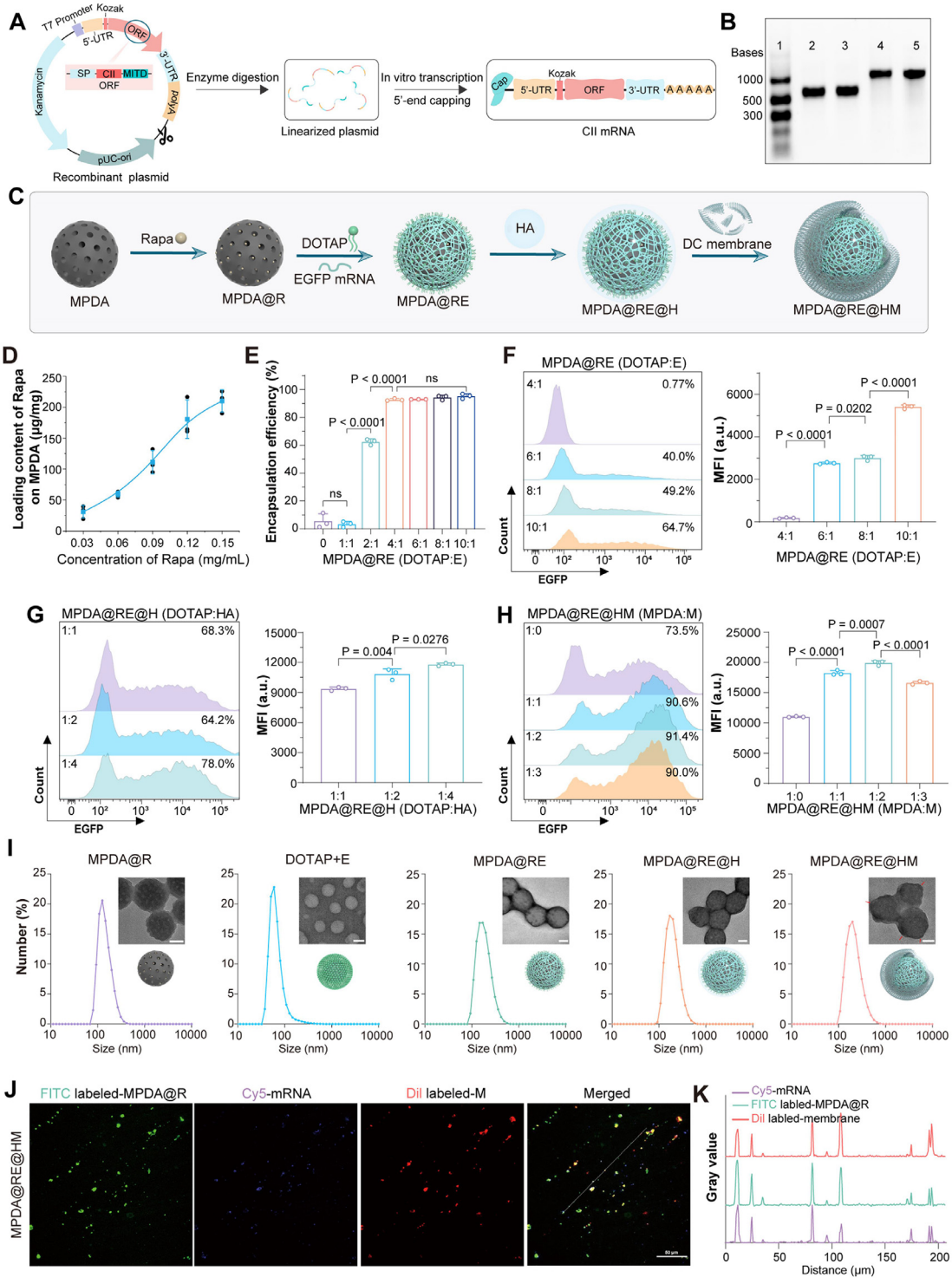


Fig. 2 – mRNA and the nanovaccine platform characterization. (A) Illustration of the recombinant plasmid template and mRNA synthesis; (B) Agarose gel electrophoresis of the designed mRNA. (Lane 1. single-stranded RNA marker; Lane 2. CII mRNA without m1-ΨTP; Lane 3. CII mRNA with m1-ΨTP; Lane 4. EGFP mRNA without m1-ΨTP; Lane 5. EGFP mRNA with m1-ΨTP; (C) Schematic illustration for the synthesis of the universal mRNA nanovaccine platform; (D) Loading efficiency of Rapa onto MPDA; (E) Encapsulation efficiency of mRNA in MPDA@RE with different mass ratios of DOTAP to mRNA measured by RiboGreen RNA reagent; Flow cytometric images and the corresponding MFI of EGFP in DC2.4 with (F) MPDA@RE, (G) MPDA@RE@H, and (H) MPDA@RE@HM treatment; (I) Hydrodynamic size of different preparations and corresponding TEM images, scale bar: 50 nm; (J) CLSM images and (K) co-localization analysis of MPDA@RE@HM labeled with FITC (MPDA@R, green), Cy5 (mRNA, purple), and DiI (DC membrane, red). All results are presented as mean ± SD, and ns means no significance.

with mRNA-mediated specific immune tolerance (Fig. 2C). Instead of CII mRNA, EGFP mRNA was utilized as a model mRNA to optimize the integration of the mRNA nanovaccine platform. Toward this end, MPDA was first synthesized *via* a nanoemulsion assembly approach [37]. The strong absorption from 400 nm to 800 nm verified the polymerization of dopamine hydrochloride under alkaline conditions, primarily confirming the successful preparation of MPDA [38] (Fig. S3A). TEM image displayed that the synthesized MPDA was uniform and spherical with mesoporous structure (Fig. S3B). Rapa was then introduced into the porous structures of MPDA to yield MPDA@R. When the final concentration of Rapa was up to 0.15 mg/ml, the loading content of Rapa on MPDA climbed to 210.07 μg/mg (Fig. 2D).

As MPDA@R was negatively charged (Fig. S12), the positively charged DOTAP was then coated on the surface of MPDA@R through electrostatic adsorption, followed by mRNA loading to obtain MPDA@RE (Fig. 2C). To maximize the transfection efficiency of the mRNA nanovaccine platform, the ratio of DOTAP to mRNA was first optimized by incubating various concentrations of DOTAP with the same amount of EGFP mRNA (DOTAP+E). The results indicated that mRNA fully hybridized with DOTAP when the DOTAP-to-mRNA mass ratio was ≥4 (Fig. S4). Moreover, the proportion of DOTAP dominated the translational capacity of mRNA when the amount of mRNA (1.25 μg/ml) was the same (Fig. S5), and the expression levels of EGFP decreased as the concentration of FBS increased. Additionally, the proportion of $EGFP^+$ cells only reached ∼65%, even when the DOTAP-to-mRNA ratio was as high as 10 and the incubation time with DC2.4 was extended to 48 h in culture medium supplemented with 10% FBS (Fig. S6). Accordingly, when the mass ratio of DOTAP and EGFP mRNA was ≥4, ∼95% mRNA was successfully loaded onto MPDA@R (Fig. 2E). Approximately 65% of MPDA@RE-treated DC2.4 exhibited EGFP fluorescence (Figs. 2F and S7), comparable to the results observed with the DOTAP+E complex. These results were attributed to the nonspecific adsorption of numerous negatively charged proteins in FBS, and the attached proteins formed a protein corona on the surface of the DOTAP and mRNA complex or MPDA@RE that interfered with cellular uptake and lysosome escape [39].

To address this issue, HA, a negatively charged natural polymer, was modified on the surface of MPDA@RE *via* electrostatic interaction to shield its positive charge. The resulting nanoparticles were defined as MPDA@RE@H (Fig. 2C). The HA dosage was then optimized by comparing the transfection efficiency of MPDA@RE@H with varying mass ratios of DOTAP and HA. As expected, when the mass ratio of DOTAP to HA was 1:4, ∼80% of DC2.4 exhibited green fluorescence (Fig. S8) and the mean fluorescence intensity (MFI) was elevated significantly (Fig. 2G), underscoring the significance of HA coating in promoting the transfection efficacy of mRNA nanovaccine.

Subsequently, the DC membrane was coated onto the outermost layer of MPDA@RE@H *via* hydrogen-bonding networks and HA-CD44 interactions [40], yielding MPDA@RE@HM to increase the cellular uptake and improve DC-targeting capability (Fig. 2C). Similarly, the optimal membrane amount was screened by the cellular EGFP expression induced by MPDA@RE@HM with different MPDA-to-membrane mass ratios. As shown in Figs. 2H and S9, EGFP expression was significantly increased following membrane modification. When the mass ratio of MPDA to membrane was set as 1:2, the proportion of $EGFP^+$ cells reached ∼91%, and MFI was close to 20,000, which was considerably higher than that of MPDA@RE@H. These results demonstrated that membrane coating further enhanced the transfection efficacy of the mRNA nanovaccine.

The designed universal mRNA nanovaccine platform MPDA@RE@HM was subsequently characterized using various techniques to obtain detailed information. Agarose gel electrophoresis assay confirmed that mRNA was successfully loaded and no free mRNA band was observed in each lane (Fig. S10). Moreover, the fabrication process had minimal influence on the stability of mRNA within MPDA@RE@HM. With the assistance of RiboGreen RNA reagent, the encapsulation rate of mRNA in the final MPDA@RE@H and MPDA@RE@HM was determined to be ∼95% (Fig. S11). Zeta potential, dynamic light scattering and TEM were further employed to analyze the morphological and structural characteristics of different nanoparticles. Fig. S12 illustrated the zeta potential variations during the synthesis process of the mRNA nanovaccine. The positive charge of MPDA@RE enabled the tight adsorption of mRNA. The HA coating effectively imparted a negative charge to MPDA@RE@H, potentially reducing the adsorption of serum proteins from FBS. Furthermore, the hydrodynamic diameter of the nanoparticles gradually increased, indicating the successful loading of each ingredient (Figs. 2I and S13). Concurrently, the morphology of the nanocarriers changed step-by-step and a distinctive multilayer structure of MPDA@RE@HM was observed compared with MPDA@RE@H. SDS-PAGE verified the presence of DC membrane proteins within MPDA@RE@HM (Fig. S14), whereas no bands were observed in the lane of MPDA@RE@H. This result suggested that the preparation process did not alter the composition of membrane proteins, which was essential to preserve the original bioactivity and function of membrane proteins. To precisely demonstrate the assembly of MPDA@RE@HM, the ingredients MPDA@R, mRNA and DC membrane were visualized by FITC, Cy5 and DiI, respectively. The fluorescent MPDA@RE@HM was then imaged by CLSM. As seen from Fig. 2J, the green signal of FITC overlapped well with the red signal of DiI and near-infrared fluorescence of Cy5. Co-localization analysis revealed that all three fluorescent signals exhibited similar profiles at the identical positions (Fig. 2K), suggesting a successful integration of MPDA@R, mRNA, and DC membrane. Noticeably, the prepared MPDA@RE@HM exhibited remarkable stability at 4 °C over 12 d as evidenced by the slight changes in particle size, polydispersity index (PDI) and zeta potential (Fig. S15).

To better understand the enhanced transfection efficacy of MPDA@RE@HM, the influences of HA and DC membrane coating on minimizing the nonspecific adsorption of serum proteins were further explored. After incubation of the different preparations with RPMI 1640 medium containing 10% FBS, the preparations were collected by centrifugation and analyzed by SDS-PAGE. As presented in Fig. S16, the grayscale of protein bands significantly diminished compared to MPDA@RE and the adsorption of proteins onto MPDA@RE@H decreased as the increase of HA amount, and

the lowest intensity of the protein bands was observed at a mass ratio of DOTAP to HA of 1:4. Given that DC membrane proteins within MPDA@RE@HM interfered with the adsorbed serum proteins, the nonspecific adsorption was calculated by deducting the gray value of MPDA@RE@HM alone. The results showed that protein adsorption of MPDA@RE@HM was further decreased compared to MPDA@RE@H. The reduced serum proteins adsorption onto MPDA@RE@HM was attributed to the reversed zeta potential from positive (MPDA@RE) to negative (MPDA@RE@H and MPDA@RE@HM) and the enhanced hydrophilicity and decreased mesoporosity of mRNA nanovaccine after HA and DC membrane coating [41].

3.2. *Intracellular behavior of the mRNA nanovaccine*

Despite the excellent transfection efficacy of the universal mRNA nanovaccine platform, the intracellular behavior in DCs was thoroughly investigated to better understand the immune-regulatory capacity and anti-inflammatory potential of the mRNA nanovaccine. Firstly, we verified that the developed mRNA nanovaccine showed no noticeable influence on the viability against normal DC2.4 and IFN-γ-induced inflammatory DC2.4 at a concentration of 5 μg/ml (based on MPDA, Fig. S17). Furthermore, none of the individual components induced a significant increase in the proportion of $CD86^{+}MHCII^{+}$ cells after 48 h of co-incubation with DC2.4 (Fig. S18), indicating a low immunogenicity of each ingredient. Therefore, the final concentration of the mRNA nanovaccine was set at 5 μg/ml, with other formulations or components matched to those in MPDA@RC@HM for subsequent cellular experiments.

To investigate the intracellular delivery of mRNA, ^{Cy5}E was utilized as a model mRNA to prepare fluorescent preparations. The intracellular uptake levels of various formulations in DC2.4 and human umbilical vein endothelial cells (HUVECs) after incubation for different periods of time were first examined. As shown in Figs. 3A, S19 and S20, the cellular uptake of the listed formulations was time-dependent, with maximum internalization observed at 4 h. DC2.4 treated with MPDA@R^{Cy5}E@HM exhibited stronger fluorescence than other groups at 2 and 4 h, which was absent in HUVECs (Fig. S20). The flow cytometric results demonstrated that DOTAP+^{Cy5}E, MPDA@R^{Cy5}E and MPDA@R^{Cy5}E@H treated cells exhibited no significant differences in fluorescence intensity at 2 h (Fig. 3B and 3C). Whereas the DC membrane-coated MPDA@R^{Cy5}E@HM treated cells exhibited the strongest fluorescence intensity at 2 h, confirming that the modification of DC membrane was crucial for enhancing the internalization, thus guaranteeing subsequent mRNA translation and antigen presentation with high efficiency.

Once entering DCs, mRNA nanovaccine is supposed to be transported to the lysosome. However, the numerous nucleases present in the lysosome may damage the structure of mRNA, resulting in less than 5% of the nucleic acid escaping from the lysosome into the cytoplasm [42]. Thus, the lysosome escape ability is decisive for the efficient transfection of the mRNA. To figure out the lysosome escape ability of the developed mRNA nanovaccine, MPDA@R^{Cy5}E@HM was co-incubated with DC2.4 for different time periods to visualize the subcellular distribution of mRNA (Fig. 3D). After co-incubation for 1 h, the red signal of mRNA (Cy5) highly overlapped with the green signal of lysosome (LysoTracker green), implying that mRNA nanovaccine first entered the lysosomes. Subsequently, the green and red fluorescent signals reached the maximum separation at 6 h. Intensity correlation quotient (ICQ) analysis [43] was further performed to analyze the colocalization ratio of red and green pixels (Fig. S21), showing a gradual increase up to 4 h, followed by a significant decrease at 6 h. These results suggested that mRNA effectively overcame lysosomal barriers and successfully entered the cytoplasm, which was primarily attributed to cationic lipid DOTAP. The positive surface charge provided by DOTAP promoted electrostatic interaction with the lysosomal membrane to disrupt membrane integrity [44]. Additionally, DOTAP produced proton sponge effect under the acidic lysosomal environment, leading to chloride influx and subsequent osmotic swelling [45]. Together, these processes facilitated the rupture of the lysosomal membrane and release of mRNA into the cytoplasm.

ROS play an important role in the maturation and differentiation of DCs. The decrease of intracellular ROS inhibits DC activation, cytokine secretion, and T cell proliferation and differentiation [46]. It is well-known that MPDA possesses the ROS scavenging ability, which is verified in the present study as well (Fig. S22), while Rapa exerts antioxidant effect through the blockage of the mTOR-mediated signal pathway [47]. Therefore, the developed mRNA nanovaccine likely exhibits immunomodulatory ability by eliminating ROS in inflammatory DCs. As expected, both MPDA and Rapa reduce the cellular ROS levels of the inflammatory DC2.4, and the ROS eliminating ability of MPDA@R was notably higher than that of MPDA and Rapa alone (Fig. 3E and 3G). Similarly, the fluorescence intensity of ROS was reduced as well in the cells treated with MPDA@RC, MPDA@RC@H and MPDA@RC@HM, concluding that the introduction of mRNA, HA and DC membrane did not influence the ROS clearance capacity of MPDA and Rapa. Accordingly, all MPDA and Rapa-containing preparations effectively reduced the ratio of $CD86^{+}MHCII^{+}$ cells compared with the IFN-γ-stimulated DC2.4 (Fig. 3F and 3H), highlighting the remarkable potential of the developed mRNA nanovaccine to reshape the tolerogenic phenotype of DCs. Compared to Rapa, MPDA@RC@HM greatly reduced the proportion of $CD86^{+}MHCII^{+}$ cells, demonstrating that the incorporation of Rapa boosted the immune tolerance capability of the developed mRNA nanovaccine, which agreed with the previous studies [23]. Meanwhile, the immunosuppressive effect of the mRNA nanovaccine on the maturation of BMDCs was confirmed as well. Consistent with the above results, the preparations containing both MPDA and Rapa showed superior inhibitory effect on LPS-induced BMDC maturation with decreasing proportion of $CD86^{+}MHCII^{+}$ cells (Fig. S23).

Overall, the enhanced cellular uptake and excellent lysosomal escape ability of MPDA@RC@HM contributed to the remarkable transfection efficacy of the developed mRNA. Furthermore, the ROS scavenging capacity of MPDA@RC@HM facilitated immunomodulation. High transfection efficiency and ROS scavenging ability of MPDA@RC@HM were conducive

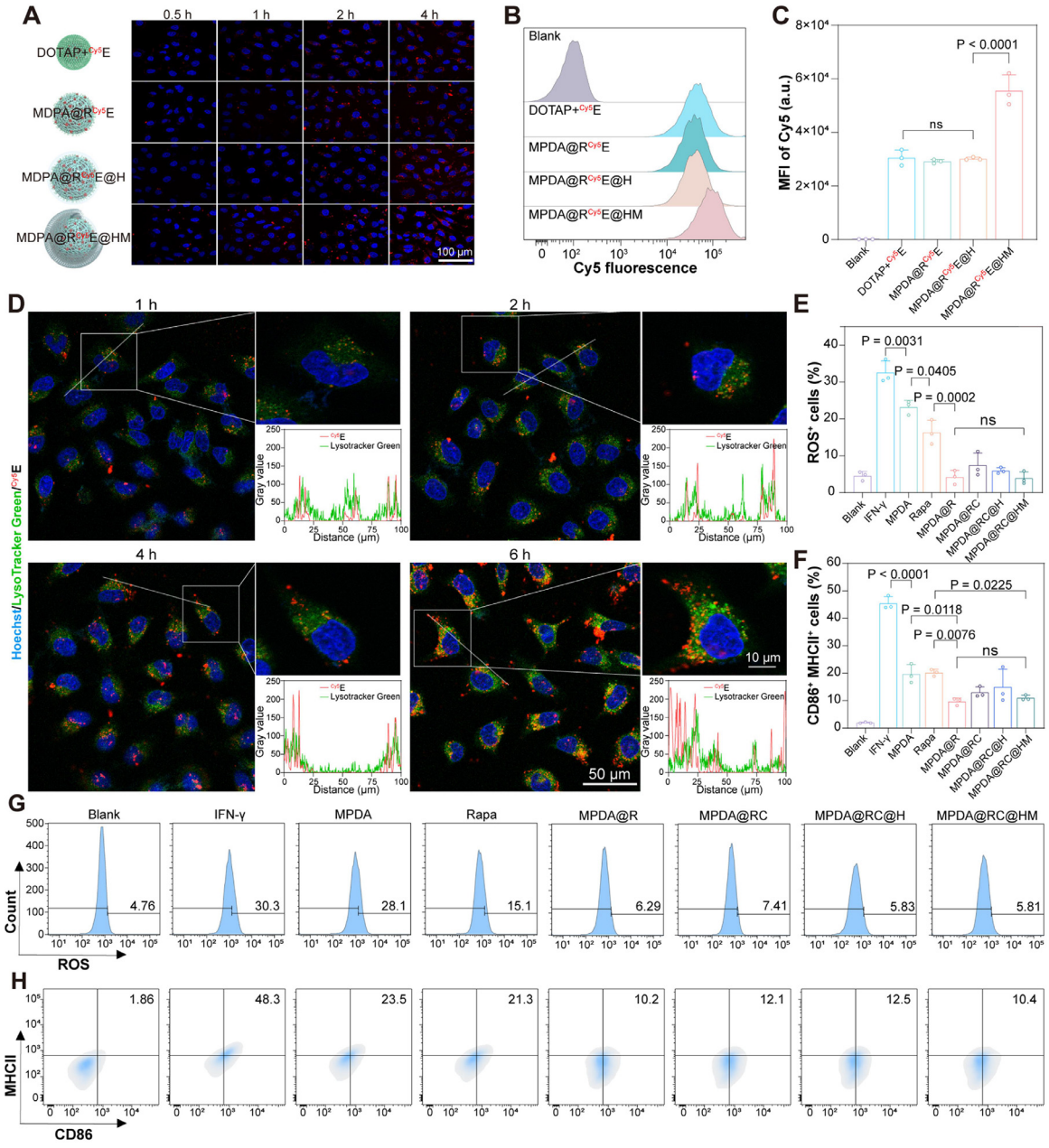


Fig. 3 – Intracellular behavior of mRNA nanovaccine in IFN-γ-induced DC2.4. (A) CLSM images of the intracellular internalization of Cy5-labeled preparations by DC2.4 at 0.5, 1, 2 and 4 h (red: ^{Cy5}E, blue: cell nucleus); (B) Flow cytometry analysis and (C) the corresponding MFI for the internalization on DC2.4 for 2 h; (D) CLSM images of Cy5-labeled MPDA@RE@HM distribution in DC2.4 at different times and the corresponding colocalization curves; (E) Quantitative analysis and (G) flow cytometry plots of ROS$^+$ cells in DC2.4; (F) Quantitative analysis and (H) flow cytometry images of CD86$^+$MHCII$^+$ cells in DC2.4. n = 3, all results are presented as mean ± SD, ns means no significance.

to achieving specific immune tolerance in the inflammatory microenvironment through efficient expression of the target antigenic peptide and inhibition of DC maturation *in vivo*.

3.3. *Anti-RA efficacy of the mRNA nanovaccine*

Encouraged by the excellent biocompatibility, transfection efficiency, and ROS scavenging capacity of the designed mRNA nanovaccine *in vitro*, its anti-inflammatory efficacy was further evaluated *in vivo*. The CIA mice model shares typical pathological features comparable to those observed in RA, such as synovial hyperplasia, monocyte infiltration and cartilage degeneration [31]. Therefore, the CIA mice model was selected to evaluate the potential anti-RA efficacy of MPDA@RC@HM. Toward this end, DBA/1 mice were injected with emulsion composed of CII and adjuvant subcutaneously at the base of the tail on Day 0 and 21, respectively (Fig. 4A). On Day 30, the mice showed loss weights, thickened paws,

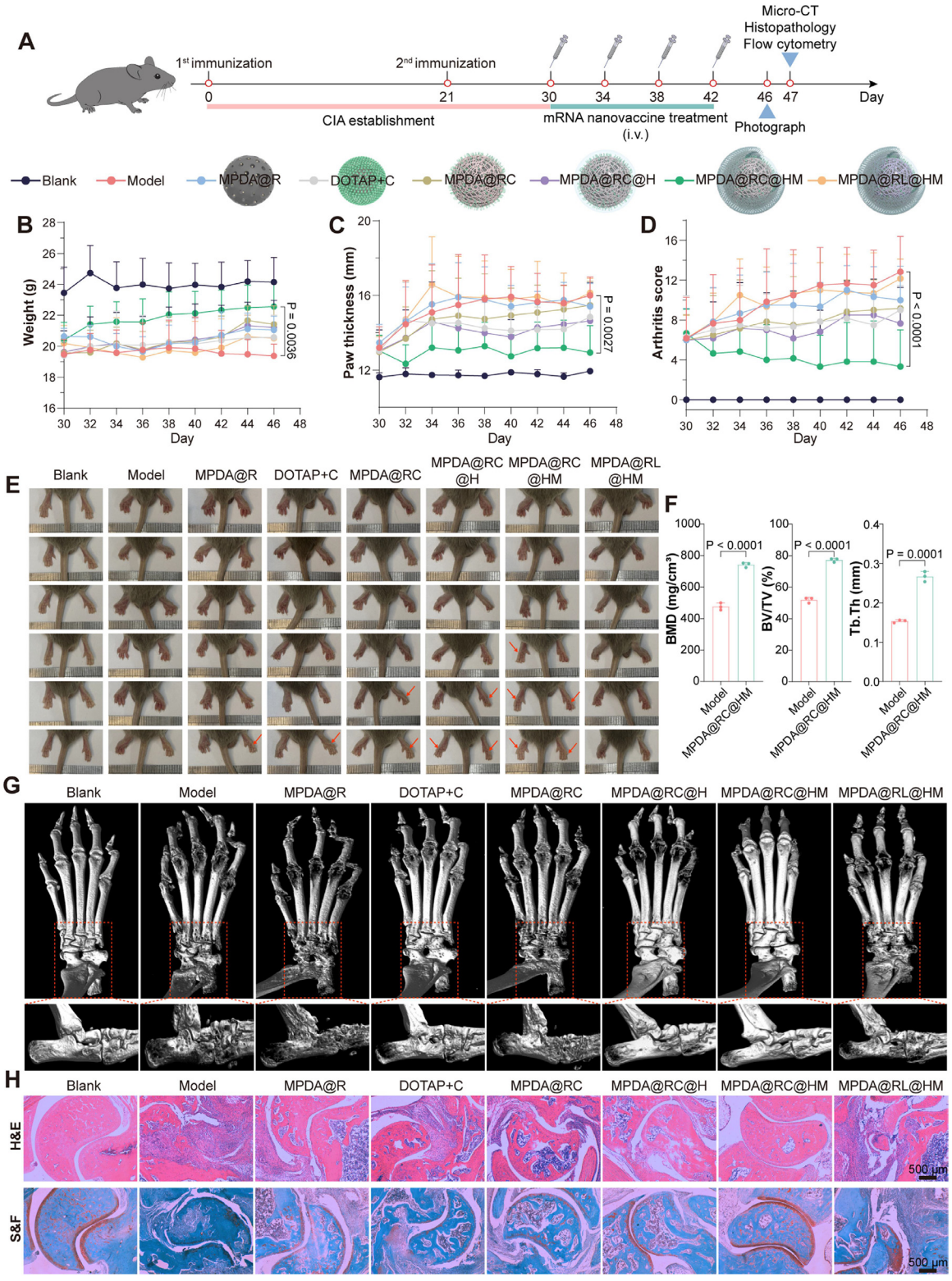


Fig. 4 – Anti-RA efficacy of mRNA nanovaccine in CIA mice. (A) Experimental schedule for CIA mice model establishment and mRNA nanovaccine administration; Fluctuations in (B) body weight, (C) paw thickness, and (D) arthritis scores of mice during the treatments ($n = 6$); (E) Images of the hind paws of the mice on Day 46, the red arrow indicates a paw with healthy morphology; (F) Statistical analysis of micro-CT images of Model and MPDA@RC@HM groups ($n = 3$); (G) Micro-CT images of the hind paws of the mice in the different treatment groups; (H) Images of H&E staining and S&F staining of the ankle joints. All results are presented as mean ± SD.

and increased arthritis scores compared with healthy mice, confirming successful establishment of the CIA model (Fig. 4B-4D). Subsequently, CIA mice were randomly divided into seven groups and administered intravenously with MPDA@R, DOTAP+C, MPDA@RC, MPDA@RC@H, MPDA@RC@HM, and MPDA@RL@HM every 4 d for a total of four injections. The healthy and untreated CIA mice were designated as the blank and model groups, respectively, while the mice treated with MPDA@RL@HM, loaded with LUC mRNA, were set as the negative control to emphasize the necessity of CII mRNA for eliciting specific tolerance therapy. During the treatment, the body weight of mice in all treatment groups recovered varying degrees, implying that the components of the mRNA nanovaccines exhibited noticeable biocompatibility and contributed to improving the health status of the CIA mice (Fig. 4B). Significant reductions in the paw thickness (Figs. 4C and S24) and arthritis score (Fig. 4D) were observed after the first dose of MPDA@RC@HM. The arthritis score of CIA mice treated with MPDA@RC@HM was further reduced to less than four on Day 46 after the fourth administration, whereas negligible or moderate reductions in arthritis score and paw thickness were observed in the CIA mice treated with other therapeutics, underscoring their limited therapeutic effects. The hind paws of mice were also photographed to record the final morphology of paws (Day 46, Fig. 4E). Specifically, three mice of the MPDA@RC@HM treatment group showed no significant difference compared with the healthy mice (blank), confirming the remarkable anti-inflammatory efficacy of MPDA@RC@HM. Interestingly, the joint symptoms of the mice in MPDA@RL@HM treated group was comparable to those of in model group, emphasizing the importance of CII mRNA in eliciting specific immune tolerance against CII.

Micro-CT was applied to visualize the bone tissue in three dimensions to further elucidate the anti-RA efficacy of MPDA@RC@HM. CIA mice in model group exhibited a severe bone erosion extending from the ankle joint to the phalange with a rough surface (Fig. 4G). The mice in the MPDA@R group exhibited considerable erosion compared with the model mice, possibly reflecting more advanced disease progression in that individual. The CIA mice treated with DOTAP+C and MPDA@RC exhibited pronounced damage in the phalange and calcaneus regions, accompanied by deformation of the skeletal architecture. The smoothness of the bones in the MPDA@RC@H treatment group was significantly improved. Moreover, negligible bone loss and smooth surface of bones were observed in the MPDA@RC@HM treated mice. In contrast, the skeletal structures of mice administered with MPDA@RL@HM, which shared the same composition as MPDA@RC@HM but had a distinct mRNA sequence, were found to be in a deteriorated state, consistent with the arthritis scores (Fig. 4D). Corresponding histomorphometric indexes obtained from Micro-CT displayed that the BMD, BV/TV and Tb.Th of the mice in MPDA@RC@HM group were 1.56-fold, 1.49-fold and 1.74-fold higher, respectively, when compared to those of mice in model group (Fig. 4F), proving that the mRNA nanovaccine exerted a beneficial influence on the bone integrity of the paw joint in CIA mice.

H&E staining was subsequently performed to evaluate the histopathology of ankle joints of CIA mice treated with various therapeutics. The joint cavity of mice in the model group showed dense infiltration of inflammatory cells, marked formation of pannus and bone erosion compared with mice in the blank group (Fig. 4H). Conversely, mice in the MPDA@RC@HM group exhibited relatively smooth cartilage and bone surfaces, along with a marked reduction in inflammatory cell infiltration within the joint cavity. Furthermore, S&F staining of ankle joint sections revealed the improvements in bone and cartilage of the CIA mice treated with MPDA@RC@HM and presented a similar result as H&E staining. Quantitative analysis of H&E and S&F staining of ankle joint sections consistently revealed that MPDA@RC@HM significantly alleviated synovial inflammation and reduced bone and cartilage erosion (Fig. S25).

3.4. *Systemic immunomodulation of the mRNA nanovaccine*

Based on the satisfactory therapeutic effects observed in inflamed joints of CIA mice, the immunomodulatory role of the mRNA nanovaccine in reshaping the splenic microenvironment and initiating systemic and local immune responses was further elucidated. On Day 47, the spleens of mice in all groups were collected, and the phenotype of T cells was quantified by flow cytometer. The proportion of Treg ($CD25^+Foxp3^+$ T cells, Fig. S26) in the MPDA@RC@H, MPDA@RC@HM and MPDA@RL@HM groups was significantly higher than that in the model group (Fig. 5A and 5B). Meanwhile, the proportion of Th17 ($CD4^+IL\text{-}17A^+$ T cells, Fig. S27), a type of T cells producing inflammatory cytokine IL-17A, in the MPDA@RC@HM group was comparable to that in the blank group (Fig. S28A and S28B). The Treg/Th17 ratio, a key immunological indicator for RA, was observed to be 14.14 times in the MPDA@RC@HM group that in the model group (Fig. S28C), suggesting that MPDA@RC@HM effectively contributed to restoring the balance of immune tolerance. Although MPDA@RL@HM improved the ratio of Treg/Th17, it failed to suppress joint inflammation induced by CII (Fig. 4D), which was probably due to the expression of an irrelevant antigen [48].

Considering the significant regulatory effect of the mRNA nanovaccine on T cells within the spleen, the level of CII antibody in the serum was next assessed to confirm the impact of nanovaccine on systemic specific antibodies. CII antibody levels in the serum of treated mice were analyzed on Day 47. As seen in Fig. 5C, the concentration of CII antibody in model mice rose to ~479,003 units/ml, confirming the significance of CII to RA development. Conversely, a significantly lower CII antibody level (~4,798 units/ml) was found in the CIA treated with MPDA@RC@HM. Meanwhile, MPDA@RL@HM loaded with unrelated mRNA hardly influenced the concentration of CII antibody, highlighting the importance of CII mRNA in inducing specific immune tolerance.

To assess the potential impact of spleen-mediated immune modulation on the inflammatory process in the joints, the cytokine balance, ROS levels and macrophage polarization in the ankle joints were examined. The mRNA levels of proinflammatory (IL-1β, IL-6 and TNF-α) and anti-inflammatory cytokine (TGF-β) at the joint lesions in each group were detected on Day 47. Compared with the model

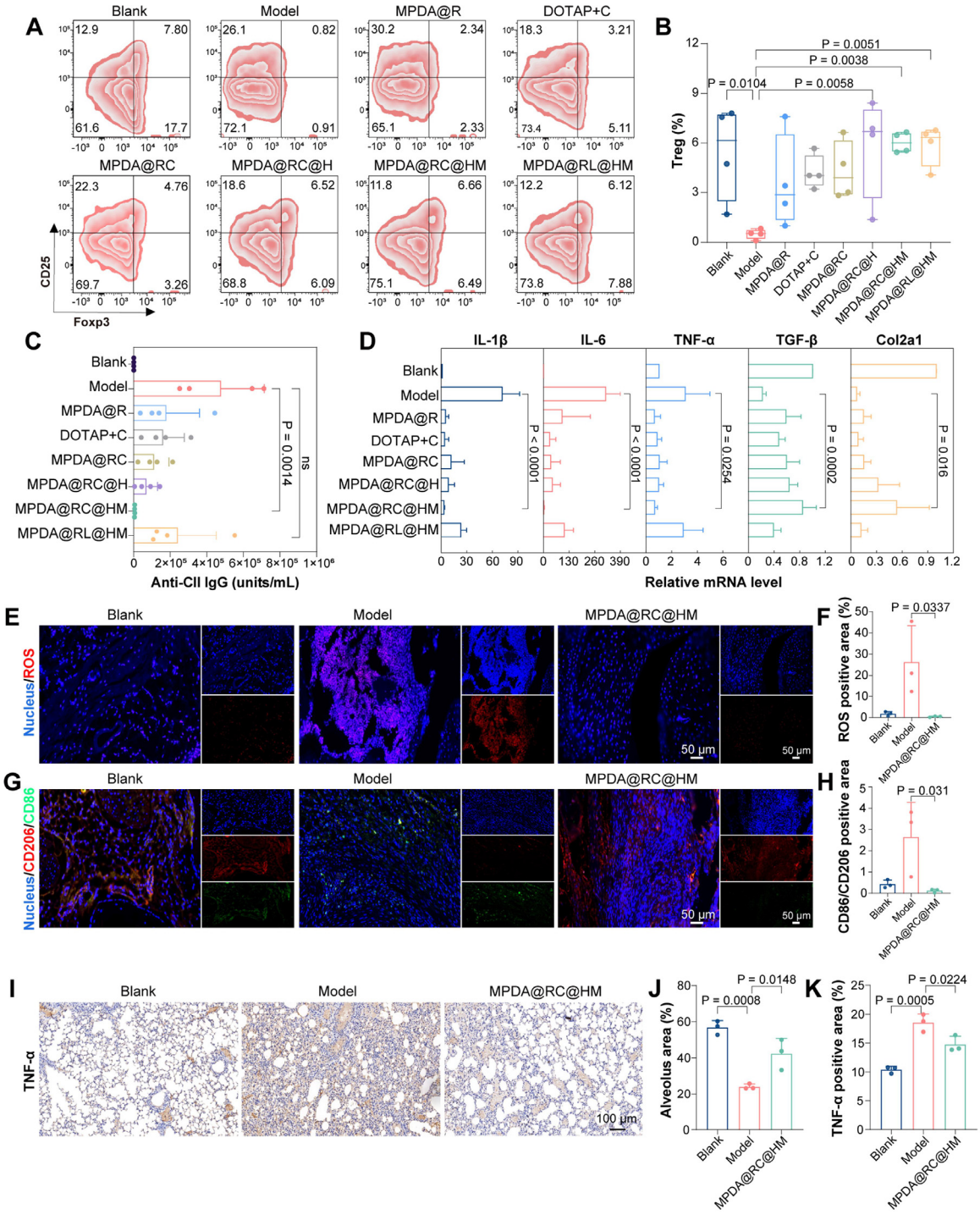


Fig. 5 – Immunomodulation by mRNA nanovaccine in CIA mice. (A) Flow cytometry plots and (B) the corresponding analysis of $CD25^{+}Foxp3^{+}$ T cells in the splenocytes ($n = 4$); (C) Concentration of CII antibody in the serum of the mice after the listed administrations ($n = 4$); (D) RT-qPCR analysis of IL-1β, IL-6, TNF-α, TGF-β and Col2a1 in the joints of mice after the various treatments ($n = 4$); (E) DHE staining of the ankle joint and (F) the corresponding quantitative analysis of ROS positive area ($n = 3$); (G) Immunofluorescence staining of CD86 (green) and CD206 (red) of the ankle joint and (H) the corresponding quantitative analysis ($n = 3$); (I) Immunohistochemical staining of TNF-α and corresponding statistical analysis of (J) alveolus area and (K) TNF-α positive area ($n = 3$). All results are presented as mean ± SD.

group, the levels of all tested pro-inflammatory cytokine genes were down-regulated, while the anti-inflammatory cytokine TGF-β gene was up-regulated in the MPDA@RC@HM group, verifying its capacity to reshape the cytokine balance in the joints of CIA mice (Fig. 5D). Moreover, a higher level of the CII gene (Col2a1) in the MPDA@RC@HM group was detected (Fig. 5D), suggesting enhanced cartilage repair. This restoration of cartilage likely resulted from the suppressed proinflammatory cytokines, which inhibited the synthesis and expression of CII in the chondrocytes [49]. The intracellular ROS in the ankle joints were visualized using DHE staining. As shown in Fig. 5E and 5F, the fluorescence intensity of DHE (red) in the model group was considerably higher than that in the MPDA@RC@HM group, and the MPDA@RC@HM group displayed a comparable fluorescence level to the blank group, confirming the ROS scavenging capacity of MPDA@RC@HM, which was consistent with the results described in Fig. 3E and 3G. Immunofluorescence staining was used to visualize CD86 and CD206 in joint slices to recognize M1 and M2 macrophages, respectively (Fig. 5G and 5H). Similar to the result of the ROS assay, MPDA@RC@HM group exhibited a noticeable reduction in CD86/CD206 ratio than model group, which played a pivotal role in inhibiting inflammation and mitigating joint destruction [50]. These results signified that the mRNA nanovaccine effectively maintained the cytokines balance, reversed the oxidative stress and reshaped the phenotype of macrophages in the joint lesions, which was beneficial for restoring local immune tolerance.

More importantly, the developed mRNA nanovaccine platform exhibited exceptional biocompatibility with minimum influences on the levels of RBC, WBC, HGB, HCT and PLT compared with the blank group (Fig. S29). Furthermore, the biosafety of the treatment was further verified by the absence of visible lesions in the major organs, including the heart, liver, spleen and kidney (Fig. S30). However, significant inflammatory damage was observed in the lung sections of CIA mice in the model group, which was subsequently confirmed by immunohistochemical staining of TNF-α (Fig. 5I-5K). Damaged alveoli and elevated TNF-α signals were observed in the lung sections of mice in the model group compared with those in the blank group, potentially attributable to the systemic inflammatory response in CIA mice. Conversely, TNF-α expression in the lungs of MPDA@RC@HM-treated mice was significantly reduced, indicating effective attenuation of pulmonary inflammation. Based on these results, we hypothesized that the mRNA nanovaccine successfully reached the lungs and exerted immune tolerance.

3.5. *Dual-targeted delivery and dual transfection of the mRNA nanovaccine in CIA mice*

To verify the above hypothesis that the mRNA nanovaccine reached the lungs, Cy5-labeled EGFP mRNA and LUC mRNA were utilized as model mRNAs to investigate the biodistribution and transfection capacity *in vivo*, respectively (Fig. 6A). The CIA model was constructed, randomly divided into four groups and administered intravenously with DOTAP+^{Cy5}E, MPDA@R^{Cy5}E, MPDA@R^{Cy5}E@H, and MPDA@R^{Cy5}E@HM, respectively. Fig. 6B and 6C demonstrated that CIA mice in the DOTAP+^{Cy5}E and MPDA@R^{Cy5}E groups exhibited stronger Cy5 signals at 2 and 4 h than the other two groups, followed by a rapid decrease of fluorescence intensity over time. The accelerated biodistribution and clearance can be attributed to the positive charge of DOTAP+^{Cy5}E and MPDA@R^{Cy5}E, which affected their distribution behavior in the mice [51]. In contrast, the Cy5 signal in MPDA@R^{Cy5}E@HM-treated mice remained relatively stable between 2 and 24 h, indicating prolonged organ retention. After 24 h of observation, the mice were euthanized and major organs were harvested for *ex vivo* imaging (Fig. 6D). The Cy5 signal in the spleen of the MPDA@R^{Cy5}E@HM group was 1.39-fold and 1.28-fold that of the MPDA@R^{Cy5}E and MPDA@R^{Cy5}E@H groups, respectively (Fig. S31), confirming that DC membrane modification promoted mRNA accumulation in the spleen. Although splenic accumulation was not markedly different between MPDA@R^{Cy5}E@HM and DOTAP+^{Cy5}E, the DC membrane coating still promoted more efficient specific cellular uptake within the DCs of the spleen (Fig. 3A-3C). Additionally, DOTAP+^{Cy5}E and MPDA@R^{Cy5}E groups exhibited higher Cy5 signal in the livers, likely due to their positive charges facilitating liver accumulation and enhancing metabolic processes [52]. Moreover, our findings revealed increased accumulation of MPDA@R^{Cy5}E@HM in the lungs (Figs. 6D and S31). This phenomenon indicated that lungs were involved in the systemic inflammatory response in CIA mice [53], contributing to the aggregation of DCs. Consequently, the DC membrane-mediated homologous targeting facilitated the accumulation of MPDA@R^{Cy5}E@HM in the pulmonary tissue.

To visualize the distribution of protein translated by the mRNA nanovaccine *in vivo*, LUC mRNA was utilized as a model mRNA to prepare DOTAP+L, MPDA@RL, MPDA@RL@H and MPDA@RL@HM and injected intravenously into CIA mice. Subsequently, D-luciferin was injected to visualize the translated LUC and the bioluminescence was captured 6 h later. As shown in Fig. 6E and 6F, the expression of the target protein in the spleen and lungs of mice in the MPDA@RL@HM group was much higher than that in the DOTAP+L, MPDA@RL, and MPDA@RL@H groups. These results were consistence with the biodistribution behavior of mRNA (Fig. 6D). Such kind of distribution and translation of the target mRNA in the spleen and lungs of CIA mice was a prerequisite for the subsequent remodeling of the tolerance phenotype of DCs, thereby specifically inhibiting the systemic inflammatory response. Simultaneously, the mRNA nanovaccine entering the lungs may exert an inhibitory effect on RA-associated pneumonia.

3.6. *Therapeutic effects of the mRNA nanovaccine on RA-associated pneumonia*

To further investigate the anti-inflammatory effect of the mRNA nanovaccine on RA-associated pneumonia, the CIA model was constructed and divided into two groups (model group: CIA mice without treatment; MPDA@RC@HM group: intravenous injection with MPDA@RC@HM). Healthy mice were set as the blank group (Fig. 7A). Consistent with the findings in Fig. 4B-4D, the designed mRNA

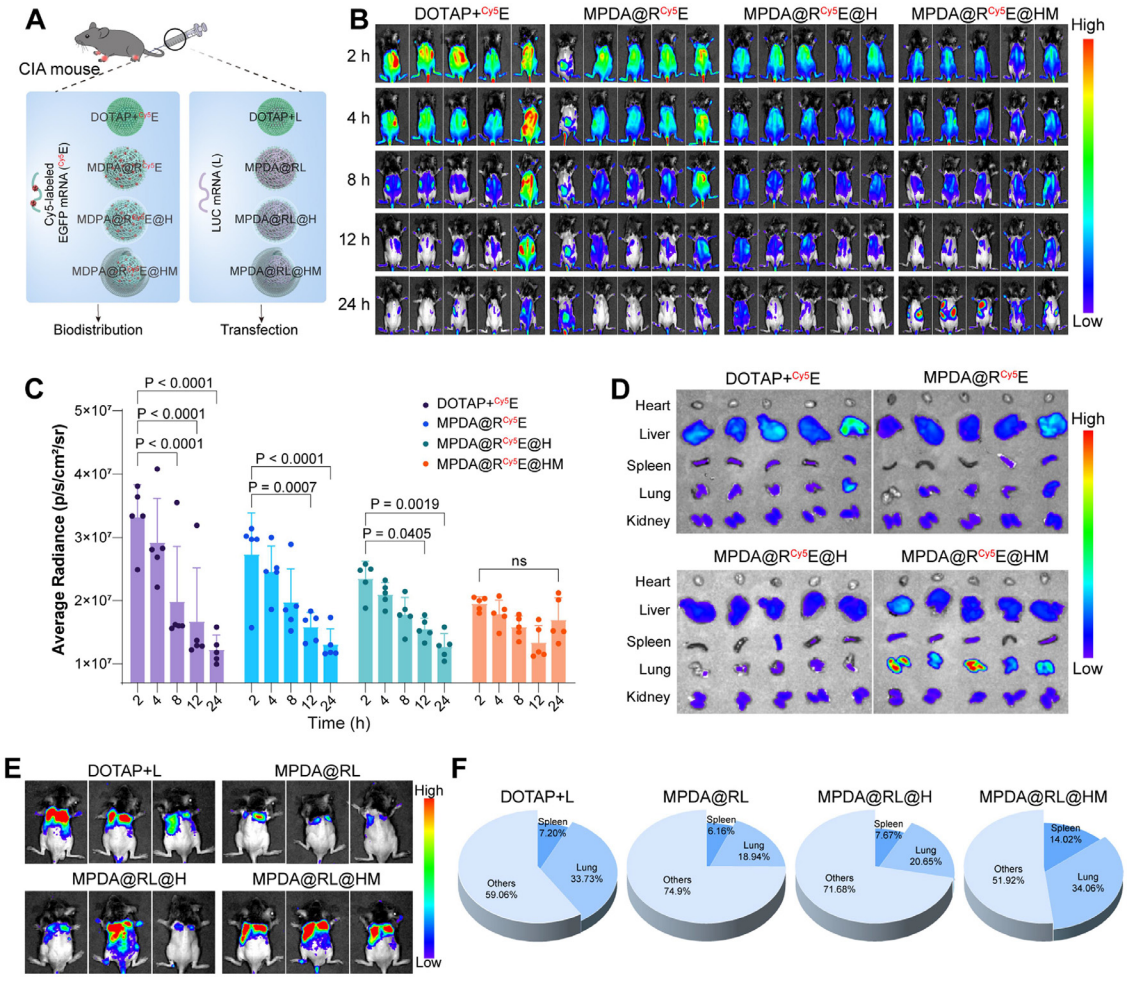


Fig. 6 – Biodistribution and transfection of mRNA nanovaccine *in vivo*. (A) Schematic illustration of the preparation and administration process of the mRNA nanovaccine; (B) Fluorescence images of CIA mice by different treatments over time monitored by the IVIS system; (C) Quantification of fluorescence intensity in the whole body at different time points ($n = 5$); (D) Fluorescence images of major organs at 24 h ($n = 5$); (E) Bioluminescence images of CIA mice 6 h post-intravenous injection ($n = 3$); (F) Proportion of bioluminescence intensity in the spleen and lungs to the total signal intensity ($n = 3$). All statistical data are presented as mean ± SD, ns means no significance.

nanovaccine MPDA@RC@HM significantly increased body weight, decreased paw thickness and arthritis scores in CIA mice after four intravenous injections (Fig. S32). Concurrently, the respiratory capacity of the mice was monitored every 2 d throughout the treatment period using an animal pulmonary function instrument (Fig. 7B). As seen in Fig. 7C and 7D, the respiratory frequency and minute ventilation of CIA mice were much lower than those of healthy mice from the onset of treatment (Day 30), proving that joint inflammation adversely impacted the respiration of CIA mice. By 42 d, MPDA@RC@HM treatment markedly enhanced the respiratory frequency and minute ventilation in comparison with the CIA mice in the model group, suggesting a significant recovery in respiratory function after three administrations. This improvement was sustained until the end of the treatment. To confirm the relationship between joint inflammation and respiratory function in CIA mice, the correlation analyses of arthritis score with respiratory frequency and minute ventilation were subsequently performed (Fig. 7E and 7F). As expected, the arthritis score of joint inflammation was negatively correlated with the respiratory frequency ($r = -0.6253$) and minute ventilation ($r = -0.6138$).

Additionally, micro-CT was performed to investigate potential histopathological changes in the lungs of mice at Day 46 (Fig. 7G). Increased texture was observed in the lung of mice in model group compared with the healthy mice. This increase was likely related to chronic pneumonia caused by systemic inflammation in CIA mice, triggering compensatory hyperplasia of lung tissue. After MPDA@RC@HM treatment, the morphology of the lung was significantly improved. H&E and Masson staining further confirmed the damaged alveolar structure, reduced alveolar area, and mild pulmonary fibrosis in the lungs of mice in model group (Fig. 7H and 7I), while the lung structure of CIA mice treated with MDPA@RC@HM was significantly improved. Moreover, ROS level of the lung in untreated CIA mice was elevated (Fig. 7J

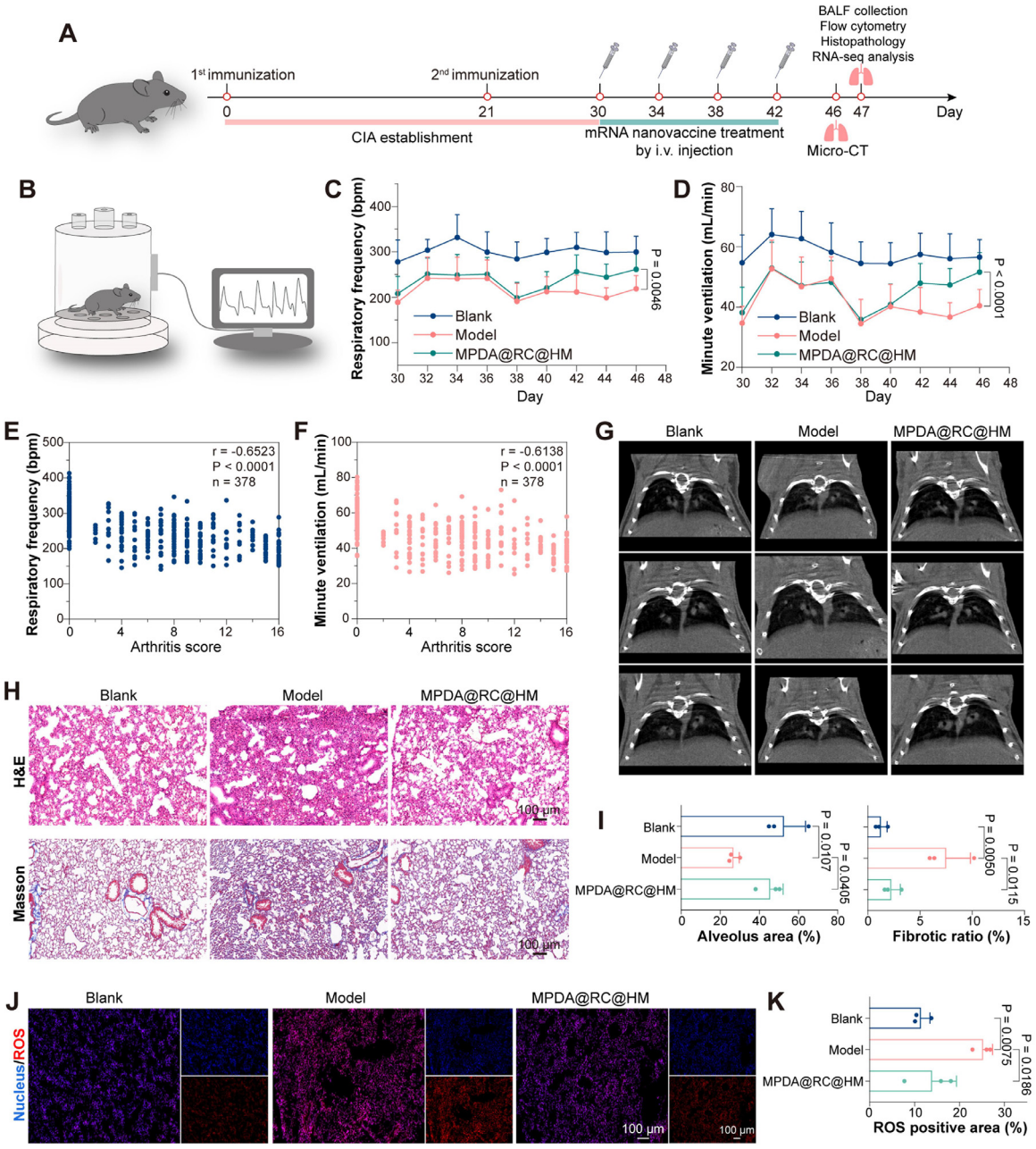


Fig. 7 – Therapeutic effects of the mRNA nanovaccine on RA-associated pneumonia. (A) Experimental schedule for CIA mouse model establishment and mRNA nanovaccine administration; (B) Schematic representation of the respiratory parameters measured in mice by a noninvasive animal pulmonary function instrument; (C) Respiratory frequency and (D) minute ventilation of DBA/1 mice monitored every 2 days (n = 14); Spearman correlation analysis of (E) respiratory frequency and (F) minute ventilation with arthritis score, respectively; (G) Micro-CT images of the lungs in the different treatment groups on Day 46 (n = 3); (H) Images of H&E staining and Masson staining in the lungs and (I) the corresponding quantitative analysis (n = 3); (J) Images of DHE staining in the lungs and (K) the corresponding quantitative analysis results of ROS positive area (n = 3).

and 7K), suggesting that the redox balance in the lungs was disrupted and caused damage to the alveolar epithelial cells. The lung in MDPA@RC@HM treated mice showed a greater attenuation of ROS level. It indicated that the mRNA nanovaccine effectively exerted antioxidant effects in the lungs, which was crucial for the repair of RA-associated pneumonia.

3.7. *Remodeling of the pulmonary microenvironment in RA-associated pneumonia*

Inspired by the efficient accumulation of the developed mRNA nanovaccine in the lungs of CIA mice and its therapeutic impact on lung pathology, the pulmonary immune microenvironment was analyzed post-treatment

to elucidate the underlying mechanism of MDPA@RC@HM against RA-associated pneumonia (Fig. 8A).

Toward this end, the total protein content and cell count in BALF were first analyzed on Day 47. As shown in Fig. 8B and 8C, the total protein content and cell number in BALF of mice in the model group were much higher than those of healthy mice in the blank group, which may be attributed to the elevated alveolar-capillary permeability associated with RA development or the accumulation of immune cells and inflammatory cytokines. Conversely, the protein level and cell count were significantly reduced after MDPA@RC@HM treatment, preliminarily suggesting an enhancement in alveolar capillary integrity or a diminished immune response within the lungs.

To further reveal the immunomodulatory effects of the mRNA nanovaccine in the lungs, the composition of immune cells including DCs, Treg and Th17 was next analyzed by flow cytometry. Compared with the immune cell constitution in the lungs of untreated CIA mice (model), the proportion of $CD86^{+}MHCII^{+}$ DCs (Figs. 8D, 8G and S33) and Th17 (Fig. 8F and 8I) was significantly decreased, while the ratio of Treg (Fig. 8E and 8H) increased in those of MDPA@RC@HM-treated CIA mice, verifying the restoration of immune tolerance in DCs and the Treg/Th17 balance after MDPA@RC@HM treatment (Fig. 8J).

RNA-seq analysis was next performed to deeply investigate the immunomodulatory mechanism of the mRNA nanovaccine on CIA-induced pneumonia at the genetic level. Principal component analysis (PCA) confirmed that the overall gene expression levels were similar within the same group but significantly different among the three groups (Fig. 8K). Subsequently, the DEGs identified from pairwise comparisons were analyzed using a Venn diagram (Fig. S34A). A heat map was then generated based on the gene sets displayed in the Venn diagram (Fig. S34B). The heat map indicated that the majority of DEG expression in MPDA@RC@HM-treated mice was reversed relative to that in untreated CIA mice (model). The volcano maps further exhibited the changes in the number and extent of DEGs for the pairwise comparisons (Fig. 8L). Specifically, the model group exhibited 1239 DEGs, with 712 upregulated genes and 527 downregulated genes compared with the blank group. Meanwhile, the MPDA@RC@HM group displayed 617 DEGs relative to the model group, comprising 374 upregulated genes and 243 downregulated genes. These results suggested that the designed mRNA nanovaccine successfully modulated gene expression during inflammation development. Subsequently, the upregulated DEGs in untreated CIA mice compared with healthy mice were subjected to KEGG pathway annotation. These upregulated genes were involved in multiple proinflammatory pathways, including cytokine-cytokine receptor interaction, NF-kappa B signaling pathway, PI3k-Akt signaling pathway, B cell receptor signaling pathway and T cell receptor signaling pathway (Fig. S35A). In addition, these upregulated DEGs were enriched in the pathways associated with RA and lung disease. Similar enrichment patterns were observed in the KEGG analysis of downregulated DEGs in the MPDA@RC@HM group compared with the model group (Fig. S35B). These findings provided preliminary genomic evidence that the CIA model induced pulmonary inflammatory responses, which were alleviated by the developed mRNA nanovaccine. The intersection of genes upregulated in the model group versus the blank group and genes downregulated in the MPDA@RC@HM group versus the model group was identified using a Venn diagram to specifically understand the activation and restoration of the immunologic process (Fig. 8M). Notably, 145 genes that were upregulated in the lungs of untreated CIA mice relative to healthy mice were reversed after mRNA nanovaccine treatment. GO annotation analysis of these 145 genes revealed that MPDA@RC@HM had significant effects on various biological processes, such as immune response, immunoglobulin production, activation and differentiation of immune cells including B cells, neutrophils and DCs (Fig. 8N).

To further elucidate the synergistic regulatory effect of the mRNA nanovaccine on multiple genes, GSEA was used to comprehensively analyze all genes in MPDA@RC@HM group versus model group. As expected, GSEA results were mainly concentrated on antioxidant activity, immune response and cytokine-related pathways. Specifically, MPDA@RC@HM group exhibited a significant upregulation in glutathione peroxidase (GPx) activity and nicotinamide adenine dinucleotide (NADH) dehydrogenase (ubiquinone) activity, along with a marked downregulation in peroxidase (POD) activity. This is likely attributed to the excellent antioxidant properties of MPDA and Rapa (Fig. S36A). Notably, the expression levels of key genes associated with GPx activity in MPDA@RC@HM group including *Gstt1, Gstp1, Gstp2, Gpx2, Gpx3, Gpx4, Gpx7, Gstm7* and *Mgst3*, were elevated compared with model group (Fig. S36B), demonstrating a recovery from oxidative stress in the tissue. Furthermore, the expression levels of nuclear genes and mitochondrial genes encoding the key subunits of NADH dehydrogenase [54] were enhanced after mRNA nanovaccine treatment, thereby maintaining electron transport and mitigating ROS production [55]. Additionally, there was a reduction in the expression of neutrophil myeloperoxidase (*Mpo*) and eosinophil peroxidase (*Epx*), which were associated with the diminished POD activity [56,57]. These results suggested that MPDA@RC@HM mitigated ROS-induced oxidative damage to lung tissue by coordinating the multiple antioxidant-related genes, aligning with the results shown in Fig. 7J and 7K. Concurrently, GSEA results also demonstrated that MPDA@RC@HM significantly downregulated the immune-related pathways (Fig. S37A). Heat map analysis of the pivotal genes involved in these immune responses revealed decreased expression levels of *Pira2* and *Lilra6* in the adaptive immune response, as well as *Cr2, Bank1* and *Lcp2* in the leukocyte activation. Additionally, a reduction was observed in *Card11* related to immunoglobulin production and *Cd79, Syk, Btk, Plcg2* and *Prkcb* in the B cell receptor signaling pathway (Fig. S37B). These results indicated that the mRNA nanovaccine effectively diminished antibody production and attenuated the immune cell response. Furthermore, multiple inflammatory cytokines, mainly produced by immune cells, were also significantly downregulated (Fig. S38A and S38B). The protein-protein interaction network was mapped based on the key genes mentioned in the GSEA analysis above, demonstrating that these genes associated with antioxidant, immune response and inflammatory cytokines interacted synergistically to facilitate the remodeling of the lung immune microenvironment (Fig. 8O).

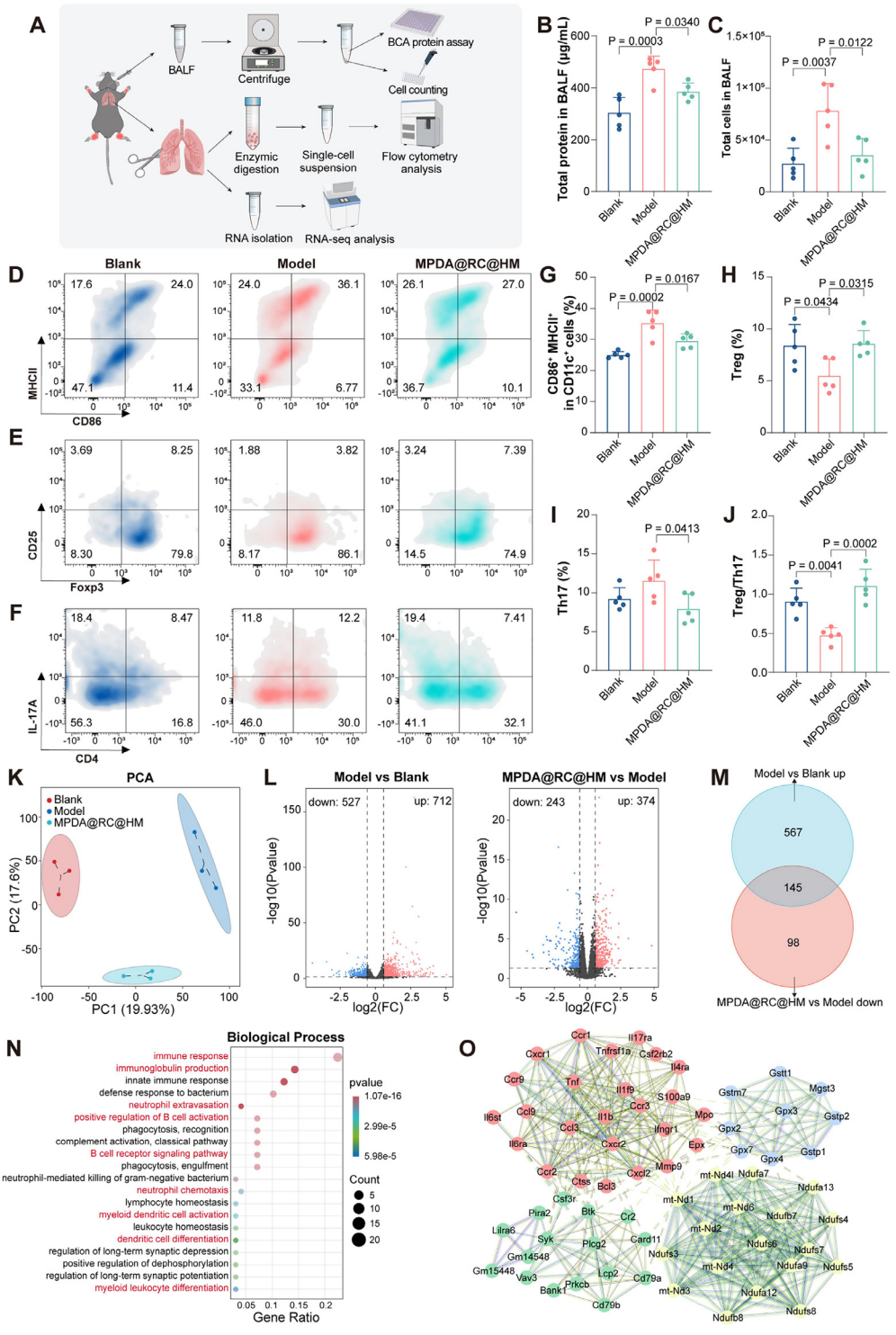


Fig. 8 – The mRNA nanovaccine-mediated immune remodeling in RA-associated pneumonia. (A) Experimental diagram of BALF detection and the immune regulation mechanism study in the lung tissue of mice; (B) Total protein concentration and (C) cell count in BALF (n = 5); (D) Flow cytometry images and (G) quantitative analysis of $CD86^{+}MHCII^{+}$ DCs (n = 5); (E) Flow cytometry images and (H) quantitative analysis of $CD25^{+}Foxp3^{+}$ T cells (n = 5); (F) Flow cytometry images and (I) quantitative analysis of $CD4^{+}IL\text{-}17A^{+}$ T cells (n = 5); (J) Ratio of Treg to Th17 (n = 5). All results are presented as mean ± SD; (K) PCA for the blank, model and MPDA@RC@HM groups (n = 3); (L) Volcano plots of DEGs for model compared with blank and MPDA@RC@HM compared with model. FC means fold change; (M) A Venn diagram illustrates the intersection of genes up-regulated in model compared with blank and genes down-regulated in MPDA@RC@HM compared with model; (N) Top 20 GO enrichment results of intersection genes in Fig. 8M; (O) Protein-protein interaction network.

3.8. Discussion

RA and RA-associated pneumonia pose a serious threat to individuals' health and lives. Due to their complexity and multidimensional features, an optimal therapeutic strategy has not been established clinically. Furthermore, RA-associated pneumonia is often inadvertently neglected and the incidence of respiratory diseases is rising, which further exacerbates the vulnerabilities of RA patients' lungs. To tackle this pressing issue, a novel mRNA nanovaccine (MPDA@RC@HM) encoding $CII_{250–270}$ epitope peptide with dual immunoregulation was successfully developed to effectively alleviate both joint inflammation and RA-associated pneumonia.

EGFP mRNA and LUC mRNA were utilized as model mRNA to construct the mRNA nanovaccine platform. The resulting mRNA nanovaccine platform exhibited efficient biodistribution and translational efficacy both in the spleen and lung, providing a solid foundation to explore its therapeutic potential in the treatment of RA and RA-associated pneumonia. The anti-RA efficacy of the mRNA nanovaccine was initially verified in CIA mice. MPDA@RC@HM treated CIA mice displayed a significant decrease in paw thickness and arthritis scores, accompanied by an augment in body weight. Further in-depth mechanistic studies revealed that the mRNA nanovaccine modulated the immune microenvironment of spleen by recovering Treg/Th17 balance, thereby maintaining both systemic and local immune balance within the joints. Similarly to the clinical manifestations of RA-ILD and the previous finding reported by Hirata et al. [53], CIA mice exhibited not only severe arthritis and bone erosion but also moderate pulmonary inflammation, which was supported by Spearman correlation analysis. In addition to the suppression on joint inflammation, MPDA@RC@HM successfully restrained CIA-associated pneumonia. RNA-seq analysis revealed that the lung microenvironment of the CIA mice was remodeled by synergically enhancing antioxidant capacity, modulating the immune cell response, and decreasing inflammatory cytokine secretion. The observed therapeutic efficacy against both RA and RA-associated pneumonia was attributed not only to successful accumulation and transfection in both the spleen and lungs but also to the synergistic effect of MPDA and Rapa, which induced antigen-specific immune tolerance. This dual immunoregulatory treatment strategy holds promise for enhancing both convenience and effectiveness in RA patient medication administration.

The therapeutic outcomes via dual immunomodulation are attributed not only to the design of the nanovaccine platform but also to the developed CII mRNA. The vaccines based on CII, whether in the form of DNA vaccines [58] or peptide vaccines [59], have demonstrated their efficacy in RA treatment. Nevertheless, DNA vaccines must undergo a series of intracellular steps to achieve therapeutic efficacy, including nuclear entry, transcription and translation, and proteolytic cleavage into peptide fragments. Peptide vaccines cannot consistently produce antigens and lack long-term immunoregulation [60]. By comparison, the mRNA vaccine designed in this work stands out with its simple structure, ease of modification, scalability for mass production and continuous translation within the host, thereby holding greater promise for clinical translation. Up to now, this is the first report on the mRNA vaccine for RA treatment. In addition, the developed nanovaccine platform based on CII mRNA is distinct from conventional LNP in that it integrates the classic cationic liposome (DOTAP) with both an ROS scavenger (MPDA) and an immunosuppressant (Rapa), thereby forming a unique system. With the help of HA, this platform overcame the transfection limitations of traditional cationic lipids in serum environments, broadening the application scope of cationic lipids. Most importantly, the engineered mRNA nanovaccine platform has broad-spectrum applicability for autoimmune diseases. By incorporating personalized mRNA that encodes pathogenic antigen peptides into this platform, it is anticipated to yield significant therapeutic benefits and hold great potential for the advancement of multivalent vaccine development. Beyond its therapeutic scope, the prophylactic potential of MPDA@RC@HM warrants further investigation. Future studies will evaluate the potential preventive effect of MPDA@RC@HM and elucidate underlying protective immune mechanisms, thereby fully exploring its value as a broad-spectrum platform for autoimmune diseases.

4. Conclusion

In conclusion, the novel mRNA nanovaccine developed in this work is capable of inhibiting RA and RA-associated pneumonia through dual immunoregulation for the spleen and lung microenvironments, offering a novel perspective for the treatment of secondary diseases of RA and autoimmune diseases.

Conflicts of interest

The authors declare that there is no conflicts of interest.

CRediT authorship contribution statement

Jingjing Su: Writing – review & editing, Writing – original draft, Validation, Methodology, Formal analysis, Data curation. **Wenguang Huang:** Validation, Formal analysis. **Wenying Zhang:** Validation, Data curation. **Ziyi Wang:** Formal analysis, Data curation. **Hongzhou Gu:** Writing – review & editing, Supervision. **Pengchao Sun:** Writing – review & editing, Supervision, Project administration, Methodology, Funding acquisition. **Yongxing Zhao:** Writing – review & editing, Supervision, Methodology, Funding acquisition, Conceptualization.

Acknowledgements

This work was supported by the National Natural Science Foundation of China (81861138004 and 81573011), the Key Scientific and Technological Project of Henan Province (252102311229), and the Modern Analysis and Computing Center of Zhengzhou University for technical assistance.

Supplementary materials

Supplementary material associated with this article can be found, in the online version, at doi:10.1016/j.ajps.2026.101120. The figures and tables with "S" before the serial number are included in the Supplementary data.

References

[1] Ding Q, Hu W, Wang R, Yang QY, Zhu ML, Li M, et al. Signaling pathways in rheumatoid arthritis: implications for targeted therapy. Signal Transduct Target Ther 2023;8(1):68.

[2] Takeuchi T. Cytokines and cytokine receptors as targets of immune-mediated inflammatory diseases—RA as a role model. Inflamm Regen 2022;42(1):35.

[3] Figus FA, Piga M, Azzolin I, McConnell R, Iagnocco A. Rheumatoid arthritis: extra-articular manifestations and comorbidities. Autoimmun Rev 2021;20(4):102776.

[4] Akiyama M, Alshehri W, Kaneko Y. Does a window of opportunity for rheumatoid arthritis-associated interstitial lung disease exist? Autoimmun Rev 2024;23(2):103501.

[5] Koduri G, Solomon JJ. Identification, monitoring, and management of rheumatoid arthritis-associated interstitial lung disease. Arthritis Rheumatol 2023;75(12):2067–77.

[6] Sebastiani M, Manfredi A, Cassone G, Sandri G, Cerri S, Ferri C. Interstitial lung disease is associated to infections of lower respiratory tract in immunocompromised rheumatoid arthritis patients. Clin Exp Rheumatol 2017;35(3):542.

[7] Kim A, Xie F, Abed OA, Moon JJ. Vaccines for immune tolerance against autoimmune disease. Adv Drug Deliv Rev 2023;203:115140.

[8] Verbeke R, Hogan MJ, Loré K, Pardi N. Innate immune mechanisms of mRNA vaccines. Immunity 2022;55(11):1993–2005.

[9] Krienke C, Kolb L, Diken E, Streuber M, Kirchhoff S, Bukur T, et al. A noninflammatory mRNA vaccine for treatment of experimental autoimmune encephalomyelitis. Science 2021;371(6525):145–53.

[10] Xu X, Wang X, Liao Y-P, Luo L, Xia T, Nel AE. Use of a liver-targeting immune-tolerogenic mRNA lipid nanoparticle platform to treat peanut-induced anaphylaxis by single-and multiple-epitope nucleotide sequence delivery. ACS nano 2023;17(5):4942–57.

[11] Zhang N, Li M, Hou Z, Ma L, Younas A, Wang Z, et al. From vaccines to nanovaccines: a promising strategy to revolutionize rheumatoid arthritis treatment. J Control Release 2022;350:107–21.

[12] Romero-Castillo L, Li T, Do NN, Sareila O, Xu B, Hennings V, et al. Human MHC class II and invariant chain knock-in mice mimic rheumatoid arthritis with allele restriction in immune response and arthritis association. Adv Sci 2024;11(23):2401513.

[13] Cho YG, Cho ML, Min SY, Kim HY. Type II collagen autoimmunity in a mouse model of human rheumatoid arthritis. Autoimmun Rev 2007;7(1):65–70.

[14] Xinqiang S, Fei L, Nan L, Yuan L, Hong X, Fang Y, et al. Construction and characterization of a novel DNA vaccine that is potent antigen-specific tolerizing therapy for experimental arthritis by increasing $CD4^+$ $CD25^+$ Treg cells and inducing Th1 to Th2 shift in both cells and cytokines. Vaccine 2009;27(5):690–700.

[15] Moten D, Teneva I, Apostolova D, Batsalova T, Dzhambazov B. Molecular mimicry of the rheumatoid arthritis-related immunodominant T-cell epitope within type II collagen (CII260-270) by the bacterial L-asparaginase. Int J Mol Sci 2022;23(16):9149.

[16] Zhu P, Li X, Ding J, Fan C, Wang Y, Wang H, et al. Simultaneous detection of DNA synthesis, activation and cytokine secretion in collagen II (250–270)-activated T lymphocytes by flow cytometry. Cell Biol Int 2004;28(11):765–72.

[17] Zhu P, Li XY, Wang HK, Jia JF, Zheng ZH, Ding J, et al. Oral administration of type-II collagen peptide 250-270 suppresses specific cellular and humoral immune response in collagen-induced arthritis. Clin Immunol 2007;122(1):75–84.

[18] Hsu JC, Liu P, Song Y, Song W, Saladin RJ, Peng Y, et al. Lymphoid organ-targeted nanomaterials for immunomodulation of cancer, inflammation, and beyond. Chem Soc Rev 2024;53(15):7657–80.

[19] Zhu M, Shi Y, Shan Y, Guo J, Song X, Wu Y, et al. Recent developments in mesoporous polydopamine-derived nanoplatforms for cancer theranostics. J Nanobiotechnol 2021;19(1):387.

[20] Wang T, Wang Y, Zhang Y, Fang Z, Li S, Gu Z, et al. Drug-loaded mesoporous polydopamine nanoparticles in chitosan hydrogels enable myocardial lnfarction repair through ROS scavenging and inhibition of apoptosis. ACS Appl Mater Interfaces 2024;16(45):61551–64.

[21] Phan NM, Nguyen TL, Min DK, Kim J. Mesoporous polydopamine nanoparticle-based tolerogenic vaccine induces antigen-specific immune tolerance to prevent and treat autoimmune multiple sclerosis. Biomaterials 2025;316:122997.

[22] Stabler CL, Li Y, Stewart JM, Keselowsky BG. Engineering immunomodulatory biomaterials for type 1 diabetes. Nat Rev Mater 2019;4(6):429–50.

[23] Jung M, Lee S, Park S, Hong J, Kim C, Cho I, et al. A therapeutic nanovaccine that generates anti-amyloid antibodies and amyloid-specific regulatory T cells for Alzheimer's disease. Adv Mater 2023;35(3):2207719.

[24] Cao Y, Long J, Sun H, Miao Y, Sang Y, Lu H, et al. Dendritic cell-mimicking nanoparticles promote mRNA delivery to lymphoid organs. Adv Sci 2023;10(33):2302423.

[25] Marchal-Sommé J, Uzunhan Y, Marchand-Adam S, Kambouchner M, Valeyre D, Crestani B, et al. Dendritic cells accumulate in human fibrotic interstitial lung disease. Am J Respir Crit Care Med 2007;176(10):1007–14.

[26] Sahin U, Derhovanessian E, Miller M, Kloke BP, Simon P, Löwer M, et al. Personalized RNA mutanome vaccines mobilize poly-specific therapeutic immunity against cancer. Nature 2017;547(7662):222–6.

[27] He Y, Zhang S, She Y, Liu Z, Zhu Y, Cheng Q, et al. Innovative utilization of cell membrane-coated nanoparticles in precision cancer therapy. Exploration 2024;4(6):20230164.

[28] He T, Tang C-k, Xu S, Moyana TN, Xiang J. Interferon gamma stimulates cellular maturation of dendritic cell line DC2.4 leading to induction of efficient cytotoxic T cell responses and antitumor immunity. Cell Mol Immunol 2007;4(2):105–11.

[29] Ge P, Chang S, Wang T, Zhao Q, Wang G, He B. An antioxidant and antibacterial polydopamine-modified thermo-sensitive hydrogel dressing for Staphylococcus aureus-infected wound healing. Nanoscale 2023;15(2):644–56.

[30] Ou Q, Zhang S, Fu C, Yu L, Xin P, Gu Z, et al. More natural more better: triple natural anti-oxidant puerarin/ferulic acid/polydopamine incorporated hydrogel for wound healing. J Nanobiotechnol 2021;19(1):237.

[31] Brand DD, Latham KA, Rosloniec EF. Collagen-induced arthritis. Nat Protoc 2007;2(5):1269–75.

[32] Qiu F, Xie D, Chen H, Wang Z, Huang J, Cao C, et al. Generation of cytotoxic aptamers specifically targeting fibroblast-like synoviocytes by CSCT-SELEX for treatment of rheumatoid arthritis. Ann Rheum Dis 2025;84(5):726–45.

[33] Konkimalla A, Konishi S, Macadlo L, Kobayashi Y,

Farino ZJ, Miyashita N, et al. Transitional cell states sculpt tissue topology during lung regeneration. Cell Stem Cell 2023;30(11):1486–1502.e9.
[34] Trapnell C, Williams BA, Pertea G, Mortazavi A, Kwan G, van Baren MJ, et al. Transcript assembly and quantification by RNA-Seq reveals unannotated transcripts and isoform switching during cell differentiation. Nat Biotechnol 2010;28(5):511–15.
[35] Kim J, Eygeris Y, Gupta M, Sahay G. Self-assembled mRNA vaccines. Adv Drug Deliv Rev 2021;170:83–112.
[36] Zhang M, Wang Y, Li B, Yang B, Zhao M, Li B, et al. STING-activating polymers boost lymphatic delivery of mRNA vaccine to potentiate cancer immunotherapy. Adv Mater 2025;37(10):2412654.
[37] Peng L, Hung CT, Wang S, Zhang X, Zhu X, Zhao Z, et al. Versatile nanoemulsion assembly approach to synthesize functional mesoporous carbon nanospheres with tunable pore sizes and architectures. J Am Chem Soc 2019;141(17):7073–80.
[38] Meng Y, Liu P, Zhou W, Ding J, Liu J. Bioorthogonal DNA adsorption on polydopamine nanoparticles mediated by metal coordination for highly robust sensing in serum and living cells. ACS Nano 2018;12(9):9070–80.
[39] Betker JL, Gomez J, Anchordoquy TJ. The effects of lipoplex formulation variables on the protein corona and comparisons with *in vitro* transfection efficiency. J Control Release 2013;171(3):261–8.
[40] Liu Z, Lin W, Liu Y. Macrocyclic supramolecular assemblies based on hyaluronic acid and their biological applications. Acc Chem Res 2022;55(23):3417–29.
[41] Mishra RK, Ahmad A, Vyawahare A, Alam P, Khan TH, Khan R. Biological effects of formation of protein corona onto nanoparticles. Int J Biol Macromol 2021;175:1–18.
[42] Mrksich K, Padilla MS, Mitchell MJ. Breaking the final barrier: evolution of cationic and ionizable lipid structure in lipid nanoparticles to escape the endosome. Adv Drug Deliv Rev 2024;214:115446.
[43] Zhang M, Shao W, Yang T, Liu H, Guo S, Zhao D, et al. Conscription of immune cells by light-activatable silencing NK-derived exosome (LASNEO) for synergetic tumor eradication. Adv Sci 2022;9(22):2201135.
[44] Fang Y, Ma B, Zhao Z, Xuan Z, Wang Y, Huang C, et al. mRNA-based FRET-FLIM imaging platform for quantifying lipid nanoparticle endosomal escape and membrane damage. J Am Chem Soc 2025;147(34):30907–23.
[45] Hanyong W, Xinyu Y, Chunyan H, Chenlu H, Hai W, Dunwan Z, et al. Programmed polymersomes with spatio-temporal delivery of antigen and dual-adjuvants for efficient dendritic cells-based cancer immunotherapy. Chin Chem Lett 2022;33(9):4179–84.
[46] Saksida T, Jevtić B, Djedović N, Miljković Đ, Stojanović I. Redox regulation of tolerogenic dendritic cells and regulatory T cells in the pathogenesis and therapy of autoimmunity. Antioxid Redox Signal 2021;34(5):364–82.
[47] Qi W, Jin L, Huang S, Aikebaier A, Xue S, Wang Q, et al. Modulating synovial macrophage pyroptosis and mitophagy interactions to mitigate osteoarthritis progression using functionalized nanoparticles. Acta Biomater 2024;181:425–39.
[48] Dangkoub F, Sankian M, Tafaghodi M, Jaafari MR, Badiee A. The impact of nanocarriers in the induction of antigen-specific immunotolerance in autoimmune diseases. J Control Release 2021;339::274–283.
[49] Kapoor M, Martel-Pelletier J, Lajeunesse D, Pelletier JP, Fahmi H. Role of proinflammatory cytokines in the pathophysiology of osteoarthritis. Nat Rev Rheumatol 2011;7(1):33–42.
[50] Cutolo M, Campitiello R, Gotelli E, Soldano S. The role of M1/M2 macrophage polarization in rheumatoid arthritis synovitis. Front Immunol 2022;13:867260.
[51] Albanese A, Tang PS, Chan WCW. The effect of nanoparticle size, shape, and surface chemistry on biological systems. Annu Rev Biomed Eng 2012;14:1–16.
[52] Cai X, Jin M, Yao L, He B, Ahmed S, Safdar W, et al. Physicochemical properties, pharmacokinetics, toxicology and application of nanocarriers. J Mater Chem B 2023;11(4):716–33.
[53] Sato T, Satooka H, Ichioka S, Maruo Y, Hirata T. Citrullinated fibrinogen is a target of auto-antibodies in interstitial lung disease in mice with collagen-induced arthritis. Int Immunol 2020;32(8):533–45.
[54] Formosa LE, Muellner-Wong L, Reljic B, Sharpe AJ, Jackson TD, Beilharz TH, et al. Dissecting the roles of mitochondrial complex I intermediate assembly complex factors in the biogenesis of complex I. Cell Rep 2020;31(3):107541.
[55] Abramov AY, Angelova PR. Cellular mechanisms of complex I-associated pathology. Biochem So Trans 2019;47(6):1963–9.
[56] Singh E, Gupta A, Singh P, Jain M, Muthukumaran J, Singh RP, et al. Exploring mammalian heme peroxidases: a comprehensive review on the structure and function of myeloperoxidase, lactoperoxidase, eosinophil peroxidase, thyroid peroxidase and peroxidasin. Arch Biochem Biophys 2024;761:110155.
[57] Roumeguère T, Noyon C, Van Antwerpen P, Poelvoorde P, Bar I, Abdulsater F, et al. Role of myeloperoxidase in ROS generation and inflammation response on prostate epithelial cells. Inflammation 2023;46(5):1859–70.
[58] Zhao X, Long J, Liang F, Liu N, Sun Y, Xi Y. Different protective efficacies of a novel antigen-specific DNA vaccine encoding chicken type II collagen via intramuscular, subcutaneous, and intravenous vaccination against experimental rheumatoid arthritis. Biomed Pharmacother 2021;144:112294.
[59] Zimmerman DH, Taylor P, Bendele A, Carambula R, Duzant Y, Lowe V, et al. CEL-2000: a therapeutic vaccine for rheumatoid arthritis arrests disease development and alters serum cytokine/chemokine patterns in the bovine collagen type II induced arthritis in the DBA mouse model. Int Immunopharmacol 2010;10(4):412–21.
[60] Qin S, Tang X, Chen Y, Chen K, Fan N, Xiao W, et al. mRNA-based therapeutics: powerful and versatile tools to combat diseases. Signal Transduct Target Ther 2022;7(1):166.